Equilibrium models of relativistic stars with a toroidal magnetic field

J. Frieben[1] and L. Rezzolla[1,2]

[1]*Max-Planck-Institut für Gravitationsphysik, Albert-Einstein-Institut, Am Mühlenberg 1, D-14476 Golm, Germany*
[2]*Department of Physics, Louisiana State University, Baton Rouge, LA 70803, USA*

ABSTRACT

We have computed models of rotating relativistic stars with a toroidal magnetic field and investigated the combined effects of magnetic field and rotation on the apparent shape (i.e. the surface deformation), which could be relevant for the electromagnetic emission, and on the internal matter distribution (i.e. the quadrupole distortion), which could be relevant for the emission of gravitational waves. Using a sample of eight different cold nuclear physics equations of state, we have computed models of maximum field strength, as well as the distortion coefficients for the surface and the quadrupolar deformations. Surprisingly, we find that non-rotating models admit arbitrary levels of magnetization, accompanied by a growth of size and quadrupole distortion to which we could not find a limit. Rotating models, on the other hand, are subject to a mass-shedding limit at frequencies well below the corresponding ones for unmagnetized stars. Overall, the space of solutions can be split into three distinct classes for which the surface deformation and the quadrupole distortion are either prolate and prolate, oblate and prolate, or oblate and oblate, respectively. We also derive a simple formula expressing the relativistic distortion coefficients, which allows one to compute the surface deformation and the quadrupole distortion up to significant levels of rotation and magnetization, essentially covering all known magnetars. Such a formula replaces Newtonian equivalent expressions that overestimate the magnetic quadrupole distortion by about a factor of 6 and are inadequate for strongly relativistic objects like neutron stars.

Key words: gravitational waves – stars: magnetars – stars: magnetic field – stars: neutron.

1 INTRODUCTION

In addition to rapid rotation, also strong magnetic fields can introduce significant deformations in neutron stars, as shown, for instance, by Bocquet, Gourgoulhon & Novak (1995) and Cardall, Prakash & Lattimer (2001), who have computed fully non-linear models of relativistic stars with a poloidal magnetic field. At the end of the collapse of the core of a massive star, differential rotation could create strong toroidal magnetic fields of the order of 10^{16}–10^{17} G inside the hot protoneutron star (Bonanno, Rezzolla & Urpin 2003; Naso et al. 2008; Bonazzola & Haensel, unpublished). As a result, realistic models of magnetized relativistic stars require the simultaneous presence of both poloidal and toroidal field components. As pointed out in Gourgoulhon & Bonazzola (1993), however, this requires a formalism capable of dealing with non-circular space–times (i.e. with convective currents in the meridional planes) like the one presented here, but which has so far been implemented only in a perturbative scheme (Ioka & Sasaki 2003, 2004). Triggered also by the increasing interest in strongly magnetized neutron stars due to their relation with soft-gamma repeaters and anomalous X-ray pulsars (Duncan & Thompson 1992; Thompson & Duncan 1996), a growing number of studies adopt-

ing perturbative techniques have appeared investigating either the field geometry and neglecting the influence of the magnetic field on the matter distribution (Ciolfi et al. 2009), or solving the coupled Einstein–Maxwell–Euler system, from which the magnetic deformation can be calculated (Ioka & Sasaki 2004; Colaiuda et al. 2008; Ciolfi, Ferrari & Gualtieri 2010; Gualtieri, Ciolfi & Ferrari 2011; Yoshida, Kiuchi & Shibata 2012). Until recently, however, fully non-linear models of relativistic magnetized stars were restricted to purely poloidal magnetic fields (Bocquet et al. 1995; Cardall et al. 2001), for which the generated space–time is circular like in the unmagnetized case (Carter 1973). Following the recent insight that also a magnetic field with only a toroidal component is compatible with the circularity of space–time (Oron 2002), studies of relativistic models of rotating stars with a toroidal magnetic field have emerged (Frieben & Rezzolla 2007; Kiuchi & Yoshida 2008; Kiuchi, Kotake & Yoshida 2009; Yasutake, Kiuchi & Kotake 2010; Yasutake, Maruyama & Tatsumi 2011). These new studies have complemented earlier Newtonian investigations (Sinha 1968; Sood & Trehan 1972; Miketinac 1973), which being simpler, allowed for the investigation of more complex field geometries, in particular of mixed poloidal and toroidal magnetic fields (Tomimura & Eriguchi 2005; Yoshida, Yoshida & Eriguchi 2006; Haskell

et al. 2008; Lander & Jones 2009; Fujisawa, Yoshida & Eriguchi 2012).

In this work, we are mainly concerned with the deformation of neutron stars endowed with a toroidal magnetic field because they might be an important source of gravitational radiation due to the prolate deformation induced by the magnetic field and provided that the axes of symmetry and of rotation are different (Bonazzola & Gourgoulhon 1996). Furthermore, Jones (1975) has pointed out that viscous processes can trigger a secular instability, which drives the axis of symmetry of the prolate star into the plane perpendicular to the angular momentum vector transforming it into a bar-shaped rotating source of gravitational radiation (Cutler 2002; Stella et al. 2005). From the astrophysical point of view, both the deformation of the stellar surface as well as the distortion of the matter distribution are relevant and can be measured by appropriate quantities, namely the surface deformation (or apparent oblateness) and the quadrupole distortion. Previous studies of relativistic models of stars with a toroidal magnetic field have provided a broad survey of non-rotating and rotating models for varying masses, radii and magnetic fluxes. The focus of this work is a complementary one to earlier studies: in order to obtain a comprehensive picture of the impact of a toroidal magnetic field on relativistic stars, we exclusively study models of fixed baryon mass corresponding to a gravitational mass of $M = 1.400\,\mathrm{M_\odot}$ in the unmagnetized and non-rotating case. Although we expect neutron stars to come in a narrow but non-zero range of masses, restricting to a single value of the gravitational mass has the important advantage that we can explore with unprecedented precision both the deformations introduced by magnetic fields and those introduced by rapid rotation. As we will comment later on, our increased accuracy has allowed us also to discover novel results and equilibrium configurations.

Our neutron stars are modelled assuming the matter to be a perfect fluid at zero temperature well described by a single-parameter equation of state (EOS), and as having infinite conductivity, as required by the ideal magnetohydrodynamics (MHD) limit. We do not consider multifluid models, which would allow for the stratification of neutron star matter, nor do we treat the protons in the interior as a superconducting fluid, which would greatly alter the magnetic properties of associated equilibrium models. Nevertheless, important results obtained for extremely magnetized models with field strengths of the order of 10^{17} G can be readily extended to configurations of much lower and more realistic field strengths of the order of 10^{13} G. More specifically, in addition to a standard $\gamma = 2$ polytropic EOS, we have considered a sample of seven realistic EOSs resulting from calculations of cold catalysed dense matter, namely the APR EOS (Akmal, Pandharipande & Ravenhall 1998), the BBB2 EOS (Baldo, Bombaci & Burgio 1997), the BN1H1 EOS (Balberg & Gal 1997), the BPAL12 EOS (Bombaci 1996), the FPS EOS (Pandharipande & Ravenhall 1989), the GNH3 EOS (Glendenning 1985) and the SLy4 EOS (Douchin & Haensel 2001). Altogether, this set of EOSs spans a wide range of physical properties and should cover any realistic description of neutron stars. For the Pol2 EOS, we have explored systematically the space of solutions and computed the corresponding surface deformation and quadrupole distortion. In addition, we have also computed the distortion coefficients, which allow one to compute the deformation of neutron stars up to large magnetizations and rotation rates through a simple algebraic expression, following the procedure devised in Cutler (2002).

The plan of the paper is the following. In Section 2, we give an overview of the novel results obtained in this study; in Section 3, we discuss the theoretical framework on which our approach, whose numerical implementation and testing is discussed in Section 4, is based. Results for static magnetized models are presented in Section 5 and that for rotating magnetized models in Section 6. In Section 7, we deal with the case of moderate magnetic field and rotation and derive empirical distortion coefficients before presenting our conclusions in Section 8.

2 GENERAL OVERVIEW

Given the complexity of the numerous results found and the risk that the most important ones may be lost in the details, in the following we briefly summarize what we believe are the most salient properties of (relativistic) stars with purely toroidal magnetic fields. We recall that we measure with ϵ_s the deformation of the surface shape, while we measure with ϵ the (quadrupolar) deviation of the matter distribution from a spherically symmetric one. Overall, equilibrium models of relativistic stars with a toroidal magnetic field exhibit the following properties.

(i) *Non-rotating* and *magnetized* models exhibit a prolate surface deformation and a prolate quadrupolar deformation, i.e. $\epsilon_s < 0$, $\epsilon < 0$, both of which decrease as the magnetization parameter λ_0 is increased.

(ii) *Rotating* and *unmagnetized* models exhibit an oblate surface deformation and an oblate quadrupolar deformation, i.e. $\epsilon_s > 0$, $\epsilon > 0$, both of which increase as the rotation frequency is increased.

(iii) Between these limiting cases, neutral lines $\epsilon_s = 0$ and $\epsilon = 0$ divide models into having prolate/oblate surface deformations and prolate/oblate internal deformations, respectively.

(iv) For *non-rotating* models no upper limit was found to the magnetization parameter λ_0, with stellar models that become increasingly prolate, but also increasingly extended as the magnetization is increased (see Figs 6 and 7).

(v) The magnetic pressure associated with the toroidal magnetic field also causes an expansion in the outer layers of the star, in particular a growth of its equatorial radius. This effect is present also for non-rotating models, for which, however, the polar radius grows more rapidly than the equatorial one, yielding a prolate surface deformation, i.e. $\epsilon_s < 0$. However, as the rotation is increased and the magnetization decreased, models can be found which have a prolate interior deformation, i.e. $\epsilon < 0$, and an oblate surface deformation, i.e. $\epsilon_s > 0$.

(vi) For any given angular velocity, the model of maximum magnetization coincides with the mass-shedding model, i.e. the model for which centrifugal and gravitational forces are equal at the equatorial radius. This point is characterized by the appearance of a cusp at the equator.

(vii) For *rotating* models the magnetic pressure at the equator adds to the centrifugal force, favouring the loss of mass. As a result of the increase in the equatorial size, the mass-shedding frequency is systematically smaller than the corresponding one for unmagnetized models.

(viii) In the space of parameters considered, the average toroidal magnetic field strength $\langle B^2 \rangle^{1/2}$ is not a monotonic function of the intrinsic magnetization parameter λ_0, and after reaching a maximum value, it gradually decreases. This implies the existence of double solutions in certain parts of the space of parameters $(\Omega^2, \langle B^2 \rangle)$.

(ix) Although the space of parameters $(\Omega^2, \langle B^2 \rangle)$ is potentially degenerate, the corresponding space of parameters (Ω^2, λ_0^2) is not. As a result, any stellar model considered is characterized uniquely by the values of the angular velocity Ω and of the magnetization parameter λ_0.
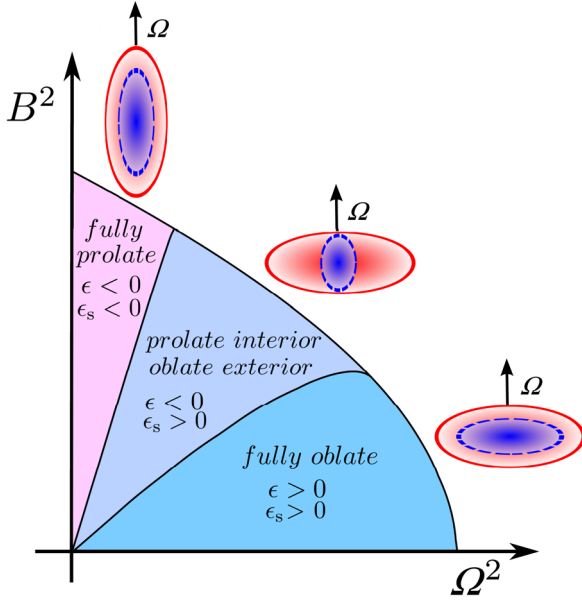
Figure 1. Schematic diagram showing the lower part of the solution space of equilibrium models in the $(\Omega^2, \langle B^2 \rangle)$ plane from the unmagnetized limit up to the maximum field-strength limit. According to the relative strength of the magnetic field and of the rotation rate, different combinations of the surface deformation, ϵ_s, and of the quadrupole deformation, ϵ, are possible.

Given these results, it is natural to divide our models into three classes: (1) models labelled PP for prolate–prolate, for which both apparent shape and matter distribution are prolate, i.e. $\epsilon_s < 0$, $\epsilon < 0$; (2) models labelled PO for prolate–oblate, whose shape is oblate whereas their matter distribution is prolate, i.e. $\epsilon_s > 0$, $\epsilon < 0$; (3) models labelled OO for oblate–oblate, which appear oblate and also exhibit an oblate matter distribution, i.e. $\epsilon_s > 0$, $\epsilon > 0$. The latter class of models had not been found by Kiuchi & Yoshida (2008). A schematic picture illustrating the three different classes for models below the maximum field-strength limit is shown in Fig. 1. Finally, while different EOSs with their different stiffness introduce quantitative differences in the behaviour described above, they all follow the same qualitative behaviour.

3 MATHEMATICAL SETUP

3.1 Basic assumptions

We assume that the space–time generated by the rotating star is *stationary* and *axisymmetric*, with Killing vector fields $\boldsymbol{e}_0$ and $\boldsymbol{e}_3$ associated with these symmetries. If, in addition, the space–time is asymptotically flat and there exists an axis where $\boldsymbol{e}_3$ vanishes, then $\boldsymbol{e}_0$ and $\boldsymbol{e}_3$ commute (Carter 1970). This enables us to choose coordinates $(x^\alpha) = (t, r, \theta, \phi)$ with vector fields $\boldsymbol{e}_0 = \partial/\partial t$ and $\boldsymbol{e}_3 = \partial/\partial \phi$. If furthermore the total stress–energy tensor $\boldsymbol{T}$ satisfies the *circularity* conditions

$$\boldsymbol{T} \cdot \boldsymbol{e}_0 = \alpha \boldsymbol{e}_0 + \beta \boldsymbol{e}_3 \,, \tag{1}$$

$$\boldsymbol{T} \cdot \boldsymbol{e}_3 = \lambda \boldsymbol{e}_0 + \mu \boldsymbol{e}_3 \,, \tag{2}$$

convective currents in the meridional planes of constant (t, ϕ) are absent by construction. In this case, quasi-isotropic (QI) coordinates can be adopted and the line element reads

$$ds^2 = g_{\alpha\beta}\, dx^\alpha dx^\beta = -N^2 dt^2 + \Phi^2 r^2 \sin^2 \theta^2 (d\phi - N^\phi dt)^2 \\ + \Psi^2 (dr^2 + r^2 d\theta^2) \,, \tag{3}$$

where N, N^ϕ, Ψ and Φ are functions of (r, θ). We further introduce the Eulerian observer $\mathcal{O}_0$ whose 4-velocity $\boldsymbol{n}$ is the future-directed unit vector normal to hypersurfaces of constant t. From equation (3), we infer $n_\alpha = (-N, 0, 0, 0)$.

The compatibility of the electromagnetic fields with the circularity condition was established long ago (Carter 1973) for the case in which the electromagnetic field tensor $\boldsymbol{F}$ is derived from a potential 1-form $\boldsymbol{A}$ with components $(A_t, 0, 0, A_\phi)$, whereas the contravariant components of the electric current vector $\boldsymbol{j}$ read $j^\alpha = (j^t, 0, 0, j^\phi)$. This fact has been exploited for computing fully relativistic models of stars with a poloidal electromagnetic field (Bocquet et al. 1995; Cardall et al. 2001). However, it has been shown that the case of a toroidal magnetic field satisfies the circularity assumption too (Oron 2002; Kiuchi & Yoshida 2008). In the following, we adopt a vector potential which is orthogonal to the Killing vectors $\boldsymbol{e}_0$ and $\boldsymbol{e}_3$, namely $\boldsymbol{A} \cdot \boldsymbol{e}_0 = 0$ and $\boldsymbol{A} \cdot \boldsymbol{e}_3 = 0$. The covariant components of $\boldsymbol{A}$ then become

$$A_\alpha = (0, A_r, A_\theta, 0) \,. \tag{4}$$

This particular form of $\boldsymbol{A}$ ensures, by construction, the absence of any poloidal electric or magnetic field component. The only non-vanishing component of the antisymmetric Faraday tensor $F_{\alpha\beta} = A_{\beta,\alpha} - A_{\alpha,\beta}$ is then given by

$$F_{r\theta} = \frac{\partial A_\theta}{\partial r} - \frac{\partial A_r}{\partial \theta} \,. \tag{5}$$

For the *electric field* $\boldsymbol{E}$ and the *magnetic field* $\boldsymbol{B}$ as measured by observer $\mathcal{O}_0$, we then obtain

$$E_\alpha = F_{\alpha\beta} n^\beta = (0, 0, 0, 0) \,, \tag{6}$$

$$\begin{aligned} B_\alpha &= -\tfrac{1}{2} \eta_{\alpha\beta\gamma\delta} F^{\gamma\delta} n^\beta \\ &= \frac{\Phi \sin \theta}{\Psi^2} \left(N^\phi \left[\frac{\partial A_r}{\partial \theta} - \frac{\partial A_\theta}{\partial r} \right], 0, 0, - \left[\frac{\partial A_r}{\partial \theta} - \frac{\partial A_\theta}{\partial r} \right] \right) \,, \end{aligned} \tag{7}$$

where $\eta_{\alpha\beta\gamma\delta}$ is the totally antisymmetric tensor associated with the metric $\boldsymbol{g}$. According to equations (6) and (7), the combination of a vanishing electric field and a toroidal magnetic field holds for *any* observer whose 4-velocity $\boldsymbol{u}$ is a linear combination of the two Killing vectors $\boldsymbol{e}_0$ and $\boldsymbol{e}_3$. The electromagnetic contribution to the stress–energy tensor is given by

$$\mathcal{T}_{\alpha\beta} = \frac{1}{4\pi} \left(F_{\alpha\kappa} F^\kappa{}_\beta - \frac{1}{4} F_{\kappa\lambda} F^{\kappa\lambda} g_{\alpha\beta} \right) \,. \tag{8}$$

Following the procedure adopted by Bonazzola et al. (1993), $\mathcal{T}$ is split up into the total electromagnetic energy density $\mathcal{E}$, the Poynting 3-vector $\mathcal{J}$ and the electromagnetic stress 3-tensor $\mathcal{S}$ as measured by the Eulerian observer $\mathcal{O}_0$. With the projection tensor $\boldsymbol{h} = \boldsymbol{g} + \boldsymbol{n} \otimes \boldsymbol{n}$, these quantities are obtained as projections of $\mathcal{T}$ on to and orthogonal to $\boldsymbol{n}$, namely $\mathcal{E} \equiv \boldsymbol{n} \cdot \mathcal{T} \cdot \boldsymbol{n}$, $\mathcal{J} \equiv -\boldsymbol{h} \cdot \mathcal{T} \cdot \boldsymbol{n}$ and $\mathcal{S} \equiv \boldsymbol{h} \cdot \mathcal{T} \cdot \boldsymbol{h}$. Specialized to the present case of no electric field and no poloidal magnetic field components, the electromagnetic contribution to the $(3 + 1)$ matter variables [for an introduction to the $(3 + 1)$ formalism of general relativity, cf. Smarr & York 1978; Gourgoulhon 2012], namely the total energy density $E \equiv \boldsymbol{n} \cdot \boldsymbol{T} \cdot \boldsymbol{n}$, the momentum density 3-vector $J \equiv -\boldsymbol{h} \cdot \boldsymbol{T} \cdot \boldsymbol{n}$ and the stress 3-tensor $S \equiv \boldsymbol{h} \cdot \boldsymbol{T} \cdot \boldsymbol{h}$ read

$$\mathcal{E} = \frac{1}{8\pi} \left(\frac{B_\phi}{\Phi\, r \sin \theta} \right)^2 \,, \tag{9}$$

$$\mathcal{J}_i = 0 \,, \tag{10}$$

$$S^r_{\ r} = \mathcal{E}\,, \quad S^\theta_{\ \theta} = \mathcal{E}\,, \quad S^\phi_{\ \phi} = -\mathcal{E}\,. \tag{11}$$

In particular, all non-diagonal components of $S^i_{\ j}$ are zero, and $S = \mathcal{E}$. The circularity assumption requires that for the Poynting vector $\mathcal{J}$

$$\mathcal{J}_r = 0\,, \qquad \mathcal{J}_\theta = 0\,, \tag{12}$$

and that the electromagnetic stress tensor S satisfies

$$S_{r\phi} = 0\,, \qquad S_{\theta\phi} = 0\,. \tag{13}$$

3.2 Einstein equations

The Einstein equations for the metric tensor g defined by equation (3) and a general stress–energy tensor T decomposed into the $(3 + 1)$ quantities E, J and S become

$$\Delta\nu = 4\pi\Psi^2(E+S) + \frac{\Phi^2 r^2 \sin^2\theta}{2N^2}(\partial N^\phi)^2 - \partial\nu\partial(\nu+\beta)\,, \tag{14}$$

$$\tilde\Delta_3(N^\phi r \sin\theta) = -16\pi\frac{N\Psi^2}{\Phi^2}\frac{J_\phi}{r\sin\theta} - r\sin\theta\,\partial N^\phi\partial(3\beta-\nu)\,, \tag{15}$$

$$\Delta_2[(N\Phi - 1)\,r\sin\theta] = 8\pi N\Psi^2\Phi\,(S^r_{\ r}+S^\theta_{\ \theta})\,r\sin\theta\,, \tag{16}$$

$$\Delta_2\zeta = 8\pi\Psi^2 S^\phi_{\ \phi} + \frac{3\Phi^2 r^2 \sin^2\theta}{4N^2}(\partial N^\phi)^2 - (\partial\nu)^2\,, \tag{17}$$

where the following abbreviations have been used:

$$\nu \equiv \ln N\,, \quad \zeta \equiv \ln(N\Psi)\,, \quad \beta \equiv \ln\Phi\,, \tag{18}$$

$$\Delta_2 \equiv \frac{\partial^2}{\partial r^2} + \frac{1}{r}\frac{\partial}{\partial r} + \frac{1}{r^2}\frac{\partial^2}{\partial\theta^2}\,, \tag{19}$$

$$\Delta_3 \equiv \frac{\partial^2}{\partial r^2} + \frac{2}{r}\frac{\partial}{\partial r} + \frac{1}{r^2}\frac{\partial^2}{\partial\theta^2} + \frac{1}{r^2\tan\theta}\frac{\partial}{\partial\theta}\,, \tag{20}$$

$$\tilde\Delta_3 \equiv \Delta_3 - \frac{1}{r^2\sin^2\theta}\,, \tag{21}$$

$$\partial a\,\partial b \equiv \frac{\partial a}{\partial r}\frac{\partial b}{\partial r} + \frac{1}{r^2}\frac{\partial a}{\partial\theta}\frac{\partial b}{\partial\theta}\,. \tag{22}$$

The resulting system of four non-linear elliptic equations for the metric variables N, N^ϕ, Ψ and Φ can be solved iteratively once suitable boundary conditions of asymptotic flatness have been adopted. Additional details can be found in Bonazzola et al. (1993).

3.3 Maxwell equations

Since the electromagnetic field tensor F is derived from a potential 1-form A, the homogeneous Maxwell equations

$$F_{\alpha\beta;\gamma} + F_{\beta\gamma;\alpha} + F_{\gamma\alpha;\beta} = 0 \tag{23}$$

are satisfied by construction. The inhomogeneous Maxwell equations $F^{\alpha\beta}_{\ \ ;\beta} = 4\pi j^\alpha$ allow us to express the electric current 4-vector j in terms of the Faraday tensor F, where the alternative expression

$$4\pi j^\alpha = \frac{1}{\sqrt{-g}}\left(\sqrt{-g}\,F^{\alpha\beta}\right)_{,\beta} \tag{24}$$

with $\sqrt{-g} = \Psi^2\Phi N r^2\sin\theta$ is used. The electromagnetic field tensor F has only one non-vanishing contravariant and covariant com-

ponent, which can now be expressed in terms of the azimuthal component B_ϕ of the magnetic field B,

$$F_{r\theta} = \frac{\Psi^2}{\Phi\sin\theta}B_\phi\,, \tag{25}$$

$$F^{r\theta} = \frac{B_\phi}{\Psi^2\Phi r^2\sin\theta}\,. \tag{26}$$

Combining equations (24) and (25), the poloidal components of the electric current 4-vector j can be written as

$$4\pi j^r = \frac{1}{\Psi^2\Phi N r^2\sin\theta}\frac{\partial(N B_\phi)}{\partial\theta}\,, \tag{27}$$

$$4\pi j^\theta = -\frac{1}{\Psi^2\Phi N r^2\sin\theta}\frac{\partial(N B_\phi)}{\partial r}\,. \tag{28}$$

The remaining components j^t and j^ϕ are zero, as expected. Note that the circularity condition, equations (1) and (2), forbids any meridional convective current contributing to J, which is ensured by assuming the charge carriers to be *massless*. By taking the divergence of equation (24), it follows that $j^\alpha_{\ ;\alpha} = 0$ thanks to the antisymmetry of F, and this continuity equation for the electric current leads to a dependence between j^r and j^θ, namely

$$\nabla\cdot j = \frac{1}{\sqrt{-g}}\left[\frac{\partial}{\partial r}(\sqrt{-g}\,j^r) + \frac{\partial}{\partial\theta}(\sqrt{-g}\,j^\theta)\right] = 0\,, \tag{29}$$

which however is trivially fulfilled by virtue of equations (27) and (28) which express j^r and j^θ as functions of a single quantity, namely $N B_\phi$, without any restriction from equation (29). A useful consequence of equations (27) and (28) is that the flow lines of the electric current coincide with the isocontours of $N B_\phi$, which allows one to visualize the current distribution without actually computing j.

3.4 Equation of motion and condition on the Lorentz force

In the case of a perfect fluid the stress–energy tensor T takes the form

$$T = (e + p)\,u\otimes u + p\,g\,, \tag{30}$$

where e is the energy density and p the pressure as measured by the *fluid comoving observer* $\mathcal{O}_1$ with 4-velocity u. Since we assume the absence of meridional currents, u can be written as a linear combination of the Killing vectors e_0 and e_3, namely

$$u = u^t e_0 + u^\phi e_3\,. \tag{31}$$

Introducing the Lorentz factor $\Gamma \equiv -n\cdot u = N u^t$ linking observers $\mathcal{O}_0$ and $\mathcal{O}_1$ and the fluid coordinate angular velocity $\Omega \equiv u^\phi/u^t$, the physical fluid velocity U and the Lorentz factor Γ can be expressed, respectively, as

$$U = \frac{\Phi r\sin\theta}{N}(\Omega - N^\phi)\,, \tag{32}$$

$$\Gamma = (1 - U^2)^{1/2}\,. \tag{33}$$

Taking into account the contribution of the magnetic field to the $(3 + 1)$ matter variables according to equations (9)–(11), the following expressions are obtained for a perfect fluid endowed with a toroidal magnetic field:

$$E = \Gamma^2(e + p) - p + \frac{1}{8\pi}\left(\frac{B_\phi}{\Phi r\sin\theta}\right)^2\,, \tag{34}$$

$$J_\phi = \Gamma^2(e + p)\Phi r\sin\theta\,U\,, \tag{35}$$

$$S^r_{\ r} = S^\theta_{\ \theta} = p + \frac{1}{8\pi}\left(\frac{B_\phi}{\Phi r\sin\theta}\right)^2\,, \tag{36}$$

$$S^\phi_\phi = p + \Gamma^2(e+p)U^2 - \frac{1}{8\pi}\left(\frac{B_\phi}{\Phi r \sin\theta}\right)^2 . \tag{37}$$

All other components are zero, and $S = 3p + \Gamma^2(e+p)U^2 + 1/(8\pi)[B_\phi/(\Phi r \sin\theta)]^2$. The projection of $\nabla \cdot \boldsymbol{T} = \boldsymbol{0}$ on to spatial hypersurfaces of constant t provides the equation of motion

$$\frac{1}{e+p}\frac{\partial p}{\partial x^i} + \frac{\partial \nu}{\partial x^i} - \frac{\partial}{\partial x^i}(\ln\Gamma) - \frac{1}{e+p}F_{i\beta}j^\beta = -F\frac{\partial\Omega}{\partial x^i}, \tag{38}$$

where F is defined as

$$F \equiv u_\phi u^t = \Gamma^2\frac{\Phi}{N}Ur\sin\theta . \tag{39}$$

Assuming a single-parameter EOS, $e = e(n)$ and $p = p(n)$, with n the baryon number density, and zero temperature, we can introduce the fluid log-enthalpy

$$H \equiv \ln\left(\frac{e+p}{n\,m_{\rm b}}\right), \tag{40}$$

with a mean baryon rest mass of $m_{\rm b} = 1.66 \times 10^{-27}$ kg. Using equations (25)–(28), (40), and discarding the case of differential rotation, equation (38) becomes

$$\frac{\partial}{\partial x^i}(H + \nu - \ln\Gamma) + \left(\frac{1}{e+p}\right)\left(\frac{1}{8\pi\Phi^2 N^2 r^2 \sin^2\theta}\right)$$
$$\times \frac{\partial(NB_\phi)^2}{\partial x^i} = 0. \tag{41}$$

Equation (41) can only be satisfied if the Lorentz force term is derived from a scalar function $\tilde{M}(r,\theta)$ as well, thus we require

$$\left(\frac{1}{e+p}\right)\left(\frac{1}{8\pi\Phi^2 N^2 r^2 \sin^2\theta}\right)\frac{\partial(NB_\phi)^2}{\partial x^i} = \frac{\partial\tilde{M}}{\partial x^i} . \tag{42}$$

Using the Schwartz theorem, the integrability condition of equation (42) can be written as

$$\frac{\partial G}{\partial\theta}\frac{\partial(NB_\phi)}{\partial r} - \frac{\partial G}{\partial r}\frac{\partial(NB_\phi)}{\partial\theta} = 0, \tag{43}$$

where $G \equiv (e+p)\Phi^2 N^2 r^2\sin^2\theta$. In other words, equation (43) states that the Jacobian of the coordinate transform $(r,\theta) \to (G, NB_\phi)$ is zero, and hence there exists a scalar function $\Theta : \boldsymbol{R}^2 \to \boldsymbol{R}$ such that $\Theta(G, NB_\phi) = 0$. Two different cases can be distinguished. (i) If $\partial\Theta/\partial(NB_\phi) = 0$, then Θ does not depend on NB_ϕ, and the relation $\Theta(G, NB_\phi) = 0$ implies that G is constant, which is equivalent to the absence of any matter and $G = 0$. (ii) If $\partial\Theta/\partial(NB_\phi) \neq 0$, then the implicit-function theorem enables us to write $NB_\phi = NB_\phi(G)$. Discarding the case without matter, we retain possibility (ii) and conclude that

$$NB_\phi = g((e+p)\Phi^2 N^2 r^2\sin^2\theta), \tag{44}$$

with g being an arbitrary scalar function. However, the regularity properties of an axisymmetric vector field in the case of spatial spherical coordinates (r,θ,ϕ) impose some further restrictions on g. For the covariant component U_ϕ of an azimuthal vector field $\boldsymbol{U} = U^\phi \boldsymbol{e}_3$, it can be shown (Bardeen & Piran 1983) that

$$U_\phi(r,\theta) = r^2\sin^2\theta\, m(r,\theta), \tag{45}$$

where m is an arbitrary axisymmetric scalar function. Application of equation (45) to NB_ϕ allows us to conclude that g can be written as $g(x) = xf(x)$, with an arbitrary regular scalar function f. The resulting expression for NB_ϕ after application of equation (45) to equation (44) reads

$$NB_\phi = (e+p)\Phi^2 N^2 r^2\sin^2\theta\, f((e+p)\Phi^2 N^2 r^2\sin^2\theta). \tag{46}$$

By inserting equation (46) into equation (42), the gradient of the magnetic potential $\tilde{M}$ reads

$$\frac{\partial\tilde{M}}{\partial x^i} = \frac{f}{4\pi}\frac{\partial}{\partial x^i}[(e+p)\Phi^2 N^2 r^2\sin^2\theta\, f] = R_i . \tag{47}$$

In general, $\tilde{M}$ cannot be determined in closed form. However, inspection of equation (47) reveals that for the sub-case of a monomial function $f(x) = \lambda_m x^m$ (not to be meant as a summation over repeated indices), a solution can be written down immediately. In this case, equation (46) simplifies to

$$NB_\phi = \lambda_m((e+p)\Phi^2 N^2 r^2\sin^2\theta)^{m+1}, \tag{48}$$

and the solution to equation (47) is given by an algebraic expression, namely

$$\tilde{M} = \frac{\lambda_m^2}{4\pi}\left(\frac{m+1}{2m+1}\right)((e+p)\Phi^2 N^2 r^2\sin^2\theta)^{2m+1} . \tag{49}$$

The simplest function f is obtained for $m = 0$ and corresponds to a constant function of value λ_0. In this case, equation (46) reduces to

$$NB_\phi = \lambda_0(e+p)\Phi^2 N^2 r^2\sin^2\theta , \tag{50}$$

and thus

$$B_\phi = \lambda_0(e+p)\Phi^2 N r^2\sin^2\theta , \tag{51}$$

supplemented by equation (49), which yields the simplified expression

$$\tilde{M} = \frac{\lambda_0^2}{4\pi}(e+p)\Phi^2 N^2 r^2\sin^2\theta . \tag{52}$$

For all models computed in this study, the magnetic field component B_ϕ is given by equation (51) and the magnetic potential $\tilde{M}$ by equation (52). Because $\tilde{M}$ vanishes on the axis of symmetry, $\tilde{M}_{\rm c} = 0$, and the integral of equation (41) reads

$$H + \nu - \ln\Gamma + \tilde{M} = H_{\rm c} + \nu_{\rm c} , \tag{53}$$

where $H_{\rm c}$ and $\nu_{\rm c}$ are the central values of H and ν, respectively. Note that a general prescription for the determination of the magnetic field B_ϕ and the magnetic potential $\tilde{M}$ can be found in Kiuchi & Yoshida (2008) and Gourgoulhon et al. (2011).

3.5 Perfect-conductor relation

According to Ohm's law and assuming an infinite conductivity for the neutron star matter, the electric field $\boldsymbol{E}'$ as measured by the fluid comoving observer $\mathcal{O}_1$ has to vanish, namely

$$E'_\alpha = F_{\alpha\beta}u^\beta = (0,0,0,0). \tag{54}$$

In the case of a purely poloidal magnetic field (Bocquet et al. 1995), the perfect-conductor relation equation (54) is non-trivial as it establishes a dependence between A_t and A_ϕ and forces a dependence of the angular velocity on A_ϕ, i.e. $\Omega = \Omega(A_\phi)$. In the case of a purely toroidal magnetic field, on the other hand, the perfect-conductor condition is trivially satisfied and no condition is set on the rotation law, so that differentially rotating models can be built as in the unmagnetized case.

It is thus possible to consider differentially rotating configurations following the procedure for the unmagnetized case. The magnetic field $\boldsymbol{B}'$ as measured by the fluid comoving observer $\mathcal{O}_1$ now becomes

$$B'_\alpha = -\frac{1}{2}\eta_{\alpha\beta\gamma\delta}F^{\gamma\delta}u^\beta$$
$$= \frac{\Gamma\Phi\sin\theta}{\Psi^2}\left(\Omega\left[\frac{\partial A_\theta}{\partial r} - \frac{\partial A_r}{\partial\theta}\right], 0, 0, -\left[\frac{\partial A_r}{\partial\theta} - \frac{\partial A_\theta}{\partial r}\right]\right). \tag{55}$$

Note that $B'_t + \Omega B'_\phi = 0$ and that $B'_\phi = \Gamma B_\phi$.

3.6 Equation of state

To solve the system of equations introduced in the previous section, we need a prescription relating the energy density e and pressure p to the baryon number density n. The simplest of such relations is offered by the polytropic EOS, in which case the following identities hold:

$$e(n) = m_{\rm b}n + \kappa \frac{n^{\gamma}}{\gamma - 1} , \tag{56}$$

$$p(n) = \kappa n^{\gamma} , \tag{57}$$

where κ is the polytropic constant and γ the adiabatic index. Combining equations (40), equations (56) and (57), the log-enthalpy H and n can be expressed as functions of each other, namely, as

$$H(n) = \ln \left(1 + \frac{\kappa}{m_{\rm b}} \frac{\gamma}{\gamma - 1} n^{\gamma - 1} \right) , \tag{58}$$

$$n(H) = \left(\frac{\gamma - 1}{\gamma} \frac{m_{\rm b}}{\kappa} (e^{H} - 1) \right) . \tag{59}$$

Hereafter, we will assume $\gamma = 2$ and refer to this EOS as to Pol2. In addition to the Pol2 EOS, we have considered a sample of seven single-constituent one-parameter EOSs treating the neutron star matter as a perfect fluid and derived from very different models of the ground state of cold (zero temperature) dense matter in this work as they are provided by the LORENE library.

More specifically, we have considered the APR EOS (Akmal et al. 1998), the BBB2 EOS (Baldo et al. 1997), the BN1H1 EOS (Balberg & Gal 1997), the BPAL12 EOS (Bombaci 1996), the FPS EOS (Pandharipande & Ravenhall 1989), the Sly4 EOS (Douchin & Haensel 2001) and the GNH3 EOS (Glendenning 1985). All of these realistic EOSs are provided in tabulated form, which requires the interpolation of listed thermodynamical quantities n, e and p between contiguous sampling points. Thermodynamical consistency of the interpolated values is ensured by an interpolation procedure based on Hermite polynomials introduced by Swesty (1996), which is crucial for the accuracy of the resulting numerical models (Salgado et al. 1994).

The properties of the spherical non-rotating and unmagnetized reference models with a gravitational mass of $M = 1.400\,{\rm M}_{\odot}$ can be found in Table 5. The softest EOS of this sample is the BPAL12 EOS, which yields the smallest circumferential radius of $R_{\rm circ} = 10.06$ km, whereas the stiffest one is the GNH3 EOS, which yields the largest circumferential radius of $R_{\rm circ} = 14.20$ km.

3.7 Global quantities

A number of global quantities which characterize the numerical models presented in this study can be computed and will be needed in the course of this investigation. These are given as follows. The gravitational mass:

$$M \equiv \int N \Psi^2 \Phi \left(E + S + \frac{2}{N} N^{\phi} J_{\phi} \right) r^2 \sin \theta \, {\rm d}r \, {\rm d}\theta \, {\rm d}\phi , \tag{60}$$

the total angular momentum:

$$J \equiv \int \Psi^2 \Phi J_{\phi} r^2 \sin \theta \, {\rm d}r \, {\rm d}\theta \, {\rm d}\phi , \tag{61}$$

the total magnetic energy:

$$\mathcal{M} \equiv \int \Psi^2 \Phi \, \mathcal{E} r^2 \sin \theta \, {\rm d}r \, {\rm d}\theta \, {\rm d}\phi , \tag{62}$$

the total kinetic energy:

$$T \equiv \frac{1}{2} \Omega J \tag{63}$$

and the gravitational binding energy:

$$W \equiv M - T - M_p - \mathcal{M} , \tag{64}$$

where the total internal energy M_p is defined as

$$M_p \equiv \int \Psi^2 \Phi \, \Gamma e \, r^2 \sin \theta \, {\rm d}r \, {\rm d}\theta \, {\rm d}\phi , \tag{65}$$

while the total baryon mass of the star is given by

$$M_{\rm b} \equiv \int \Psi^2 \Phi \, \Gamma n \, r^2 \sin \theta \, {\rm d}r \, {\rm d}\theta \, {\rm d}\phi . \tag{66}$$

Other important quantities that are more closely related to the deformation of the star are the circumferential radius $R_{\rm circ}$, which is defined through the stellar equatorial circumference as measured by the observer $\mathcal{O}_0$ and is related to the equatorial coordinate radius R according to

$$R_{\rm circ} \equiv \Phi(R, \pi/2) \, R , \tag{67}$$

the surface deformation (or apparent oblateness)

$$\epsilon_{\rm s} \equiv r_{\rm e}/r_{\rm p} - 1 , \tag{68}$$

where $r_{\rm e}$, $r_{\rm p}$ are the equatorial and polar coordinate radii, respectively, and the quadrupole distortion ϵ of the star (Bonazzola & Gourgoulhon 1996):

$$\epsilon \equiv -\frac{3}{2} \frac{\mathcal{I}_{zz}}{I} , \tag{69}$$

where $\mathcal{I}_{zz}$ is the quadrupole moment measured in some asymptotically Cartesian mass-centred coordinate system (Thorne 1980), while the moment of inertia $I = I_{zz}$ is defined as $I \equiv J/\Omega$. We stress that no moment of inertia other than the latter can be defined in a meaningful way for axisymmetric rotating bodies and that the rotation must be rigid and about the axis of symmetry. Furthermore, we note that $-(3/2)\mathcal{I}_{zz}$ differs from the standard quadrupole moment Q and that in the case of QI coordinates, the latter can be read off from the asymptotic expansion of $\ln N$ according to

$$\ln N = -\frac{M}{r} + \frac{M^2}{12r^3} + \frac{Q}{r^3} P_2(\cos \theta) + \cdots . \tag{70}$$

Thorne's quadrupole moment $\mathcal{I}_{zz}$ is the relevant quantity when the gravitational-wave emission from a distorted star has to be determined, and the corresponding values are extracted from the asymptotic expansion of certain components of the metric tensor **g** in QI coordinates following the procedure presented in Bonazzola & Gourgoulhon (1996).

4 NUMERICAL IMPLEMENTATION AND TESTS

4.1 Numerical scheme

The analytic scheme presented in Section 3 has been implemented by extending an existing multidomain, surface-adaptive spectral method for unmagnetized relativistic stars presented in Bonazzola, Gourgoulhon & Marck (1998), Gourgoulhon et al. (1999) and part of the LORENE[1] C++ class library for numerical relativity. We refer to Bonazzola et al. (1998) and Gourgoulhon et al. (1999) for a detailed

---

[1] http://www.lorene.obspm.fr

Table 1. Comparison of results for the normalized oblateness ϵ_s/h computed in the Newtonian limit for various polytropic EOSs with results from Sood & Trehan (1972) [values for ϵ/h from table 1 of Sood & Trehan (1972) where $\epsilon = (r_e - r_p)/r_0$ and r_0 is the radius of the unperturbed model]. The perturbation parameter $h = \lambda_0^2/(4\pi^2)$ is a measure of the strength of the magnetic field.

	γ	2	5/3	3/2	4/3	9/7
Sood & Trehan (1972)	(ϵ/h)	−0.213 77	−0.142 84	−0.092 92	−0.033 74	−0.017 24
This work	(ϵ_s/h)	−0.213 76	−0.142 18	−0.092 92	−0.033 74	−0.017 24

description of the numerical method and of the tests carried out. The numerical solution is computed by iteration, starting from crude initial conditions of a parabolic log-enthalpy profile, no rotation, flat space and no magnetic field. Convergence is monitored by computing $||H_n - H_{n-1}||/||H_{n-1}||$ where $||H_{n-1}||$ is the sum of the absolute values of the log-enthalpy H over all collocation points at iteration step $n - 1$. A convergent solution is assumed to be found when the normalized log-enthalpy residual decreases below a prescribed threshold, which is usually chosen to be of the order of 10^{-8} or smaller. The computational domain is divided into a spherical nucleus containing the star and two shells covering the exterior, where the last one maps on to a finite interval the whole exterior space, from a certain radius R up to spatial infinity. The default number of collocation points used in our study has been $n_\theta = 17$ in the angular direction and $\mathbf{n}_R = (33, 33, 17)$ in the radial direction, where the different numbers refer to the nucleus and the two shells, respectively. However, depending on the circumstances, the numerical resolution has been increased when necessary, i.e. up to $n_\theta = 129$ and $\mathbf{n}_R = (257, 257, 129)$ in the case of huge models with a matter distribution strongly deviating from a spherical one (cf. Table 3 and Fig. 6).

4.2 Comparison with Newtonian results

The results of the numerical scheme in the Newtonian limit have been compared with those of an earlier investigation in the Newtonian regime. Sood & Trehan (1972) have in fact computed linear perturbations of polytropic stars induced by a toroidal magnetic field corresponding to the Newtonian limit of equation (51), namely

$$\frac{B_\phi}{r \sin\theta} = \lambda_0 \, \rho \, r \sin\theta \,, \qquad (71)$$

where ρ denotes the Newtonian mass density. In Table 1, we show normalized values of the resulting oblateness for different adiabatic exponents produced with the present code and the corresponding results from Sood & Trehan (1972). We note that Sood & Trehan (1972) measured the deformation as $\epsilon_s = (r_e - r_p)/r_0$ where r_0 is the radius of the unperturbed model. Values computed according to this definition coincide with $\epsilon_s = r_e/r_p - 1$ within the rounding error of tabulated values. Clearly, for the perturbation parameter $h = \lambda_0^2/(4\pi^2)$, the respective values of ϵ_s/h agree to within 10^{-5}, except for $\gamma = 5/3$, for which the difference is about 10^{-3}. However, for $\gamma = 5/3$, certain functions intervening in the solution of the perturbed Lane–Emden equation become singular at the surface of the star (Das & Tandon 1977), suggesting a larger numerical error for the $\gamma = 5/3$ case as computed by Sood & Trehan (1972).

4.3 Virial identities

In order to monitor the global error of the numerical models computed with the new code we have calculated the two general-relativistic virial identities GRV2 (Bonazzola 1973; Bonazzola & Gourgoulhon 1994) and GRV3 (Gourgoulhon & Bonazzola 1994).

We recall that these identities have to be fulfilled by any solution to the Einstein equations equations (14)–(17) and are not enforced during the iterative procedure that leads to the solution. The GRV2 identity, in particular, has been shown to be directly related to the global error of a numerical solution (Bonazzola et al. 1993), while the GRV3 identity is an extension of the virial theorem of Newtonian physics to general relativity [see Nozawa et al. (1998) for details of the practical implementation]. For strongly magnetized non-rotating models based on a polytropic EOS with $\gamma = 2$ and the moderate number of collocation points specified in Section 4.1, the violations to the identities GRV2 and GRV3 have been found to be of the order of 10^{-6} or better. For the huge models listed in Table 3, corresponding values are of the order of 10^{-4} which required the number of collocation points to be multiplied by a factor of 8 compared to their default values. In the case of rapid rotation, on the other hand, the numerical grid is not perfectly adapted to the stellar surface, and the spectral approximation suffers from Gibbs phenomena, as reported in Bonazzola et al. (1993). However, the corresponding values of the identities GRV2 and GRV3 are still of the order of 10^{-5}. For realistic EOS, values of GRV2 and GRV3 are of the order of 10^{-4} or better.

5 NON-ROTATING MAGNETIZED MODELS

Non-rotating models of neutron stars with a toroidal magnetic field always generate *static* space–times for which the time Killing vector $\mathbf{e}_0$ is hypersurface-orthogonal. Note that this assumption does not always hold in the case of a poloidal magnetic field because the additional presence of an electric field gives rise to an azimuthal Poynting vector [cf. Bonazzola et al. (1993)], which introduces a non-zero angular momentum even when the star does not rotate. As a consequence, the shift vector component N^ϕ does not vanish.

Although we are interested in the construction of rapidly rotating models (that we will present in Section 6), non-rotating configurations allow us to investigate the effects of the magnetic field without the influence of rotationally induced effects. As a representative example, Fig. 2 shows isocontours of the magnetic field strength and baryon number density for the non-rotating model PP-Pol2 built with the Pol2 EOS and for the maximum field strength (the physical properties of model PP-Pol2 are listed in Table 4). The unmagnetized reference model with a circumferential radius of $R_{circ} = 12.00\,km$ is symbolized by a grey disc. In agreement with the simple structure function defined in equation (51), the toroidal magnetic field shown in the left-hand panel vanishes on the axis of symmetry, reaches a maximum value of $B_{max} = 7.408 \times 10^{17}\,G$ in the equatorial plane deep inside the star and decreases towards the surface of the star, where it vanishes, so that the magnetic field is fully contained inside the star. The forces exerted by the magnetic field can be visualized through the magnetic potential $\tilde{M}$, which shows a distribution similar to that of the magnetic field strength and that, for this reason, we do not report here. It should be noted that the magnetic potential $\tilde{M}$ is *repulsive* since it is positive
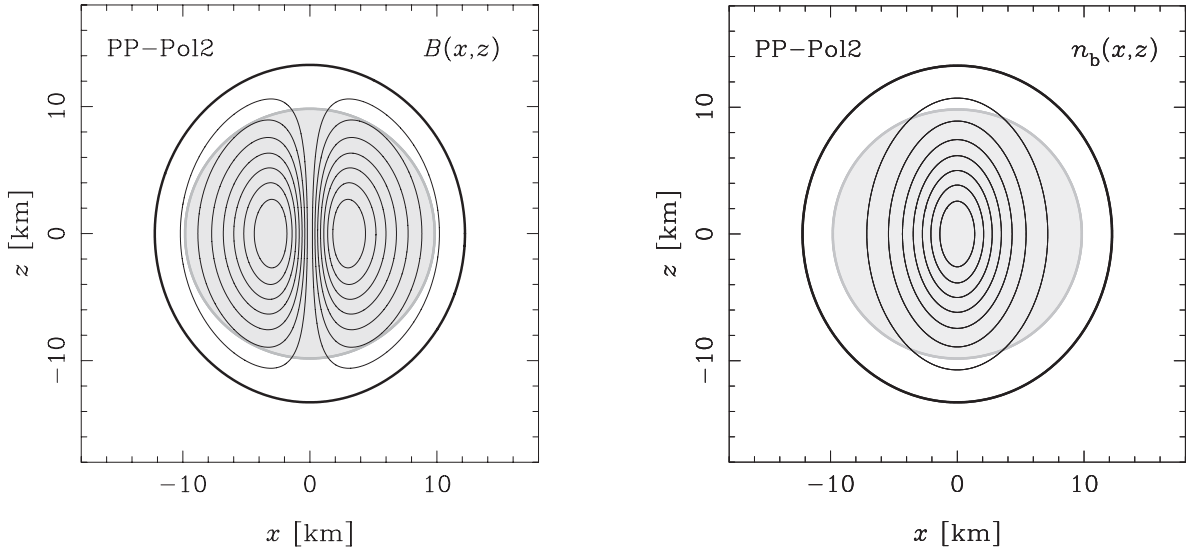
Figure 2. Isocontours of magnetic field strength (left-hand panel) and baryon number density (right-hand panel) in the (x, z) plane of model PP-Pol2 of a non-rotating star with a gravitational mass of $M = 1.400\,\mathrm{M_\odot}$ and a circumferential radius of $R_{\mathrm{circ}} = 12.00$ km in the unmagnetized case built with a polytropic EOS with $\gamma = 2$ for a maximum average magnetic field strength of $\langle B^2 \rangle^{1/2} = 2.917 \times 10^{17}$ G. The grey disc indicates the dimensions of the unmagnetized reference model. Physical properties of model PP-Pol2 are listed in Table 4.

everywhere by construction. This is to be contrasted with the magnetic potential associated with the purely poloidal magnetic field adopted in Bocquet et al. (1995), that was instead *attractive*. As a result, the corresponding forces are the opposite, despite the isocontours appear to be very similar. Note also that in the present case of a purely toroidal magnetic field defined according to equation (51), the isocontours of $\tilde{M}$ coincide with the flow lines of the electric current $\boldsymbol{j}$, which are nested loops in the meridional plane. Finally, we note that $\tilde{M}$ vanishes at the surface of the star, implying that the latter coincides with an isosurface of the gravitational potential ν, as required by equation (53) when $\ln \Gamma = 0$ and $\tilde{M} = 0$.

The forces that can be derived from $\tilde{M}$ vanish on the axis of symmetry and reach their maximum in the equatorial plane. Between the centre of the star and the maximum of $\tilde{M}$, they are directed inwards, inducing an approximately cylindrical compression of the central region of the star, which responds by a prolate deformation visible in the right-hand panel of Fig. 2. In the outer layers of the star, on the other hand, the magnetic forces are directed radially outward, pushing them away from the centre, which results in a growth of the dimensions of the star whose circumferential radius has increased now to a value of $R_{\mathrm{circ}} = 14.34$ km.

Both the apparent shape and the matter distribution are prolate, corresponding to negative values of the surface deformation and of the quadrupole distortion, namely $\epsilon_s = -0.0806$ and $\epsilon = -0.1986$, respectively. The value of ϵ_s is significantly smaller than that of ϵ, and this is due to the fact that terms of higher order in the multipole expansion of the gravitational potential ν fall off rapidly while, at the same time, the surface of the star must coincide with an isosurface of ν. This interpretation is supported by the fact that this difference is significantly smaller for small perturbations around this model, as confirmed by comparing values of respective distortion coefficients b_B and c_B reported in Section 7.

The strength of the magnetic field is controlled by the magnetization parameter λ_0 (cf. equation 52), and the physical quantities associated with our models can be parametrized accordingly, in particular the maximum magnetic field strength B_{max}. In Fig. 3, we compare our results with those reported in fig. 6 of Kiuchi &

Yoshida (2008),[2] considering in particular the variation of the gravitational mass M, of the circumferential radius R_{circ}, of the central baryon number density $n_{\mathrm{b,c}}$ and of the mean deformation $\bar{e}$. The comparison is made as a function of the maximum magnetic field strength B_{max} and for a non-rotating reference model built with the Pol2 EOS and having a baryon mass of $M_{\mathrm{b}} = 1.680\,\mathrm{M_\odot}$ and a circumferential radius of $R_{\mathrm{circ}} = 14.30$ km in the unmagnetized case. For each of these quantities χ, we define the difference as $\Delta\chi(B_{\mathrm{max}}, M_{\mathrm{b}}) \equiv [\chi(B_{\mathrm{max}}, M_{\mathrm{b}}) - \chi(0, M_{\mathrm{b}})]/\chi(0, M_{\mathrm{b}})$. We note that in Kiuchi & Yoshida (2008) the mean deformation is defined as $\bar{e} \equiv (I_{zz} - I_{xx})/I_{zz}$, where I_{xx} and I_{zz} are the moments of inertia relative to the corresponding axes (cf. equation 3.12 of Kiuchi & Yoshida 2008); this measure is similar but different from our measure of the quadrupole distortion ϵ.[3]

The most prominent feature of this comparison is that B_{max} is not a monotonic function of λ_0, thus being responsible for the presence of a turning point located at a magnetic field strength of $B_{\mathrm{max}} = 6.141 \times 10^{17}$ G. While our results (blue solid lines) agree qualitatively with those of Kiuchi & Yoshida (2008) (red dashed lines), we find significant quantitative differences for all of the quantities considered, the largest one being an increase in $n_{\mathrm{b,c}}$ of 7 per cent against the smaller 3 per cent increase found by Kiuchi & Yoshida (2008). Another important difference is in the values of the maximum magnetic field strength, which is $B_{\mathrm{max}} = 6.141 \times 10^{17}$ G for us and $B_{\mathrm{max}} = 5.503 \times 10^{17}$ G for Kiuchi & Yoshida (2008). The differences between the two calculations are smaller when comparing the mean deformations $\bar{e}$, but only for moderate values of B_{max}. Furthermore, the measure of $\bar{e}$ is considerably different from the quadrupole deformation ϵ (green dotted line), suggesting that the definition of $\bar{e}$ is not suitable for estimating the gravitational-wave

[2] The data from fig. 6 of Kiuchi & Yoshida (2008) have been read off with the utility G3DATA, see https://github.com/pn2200/g3data.
[3] More specifically, the definition of $\bar{e}$ is valid only in a Newtonian framework, where $(I_{zz} - I_{xx})/I_{zz} = (I - I_{xx})/I = Q_{\mathrm{Newt}}/I$, and Q_{Newt} is the Newtonian quadrupole moment.
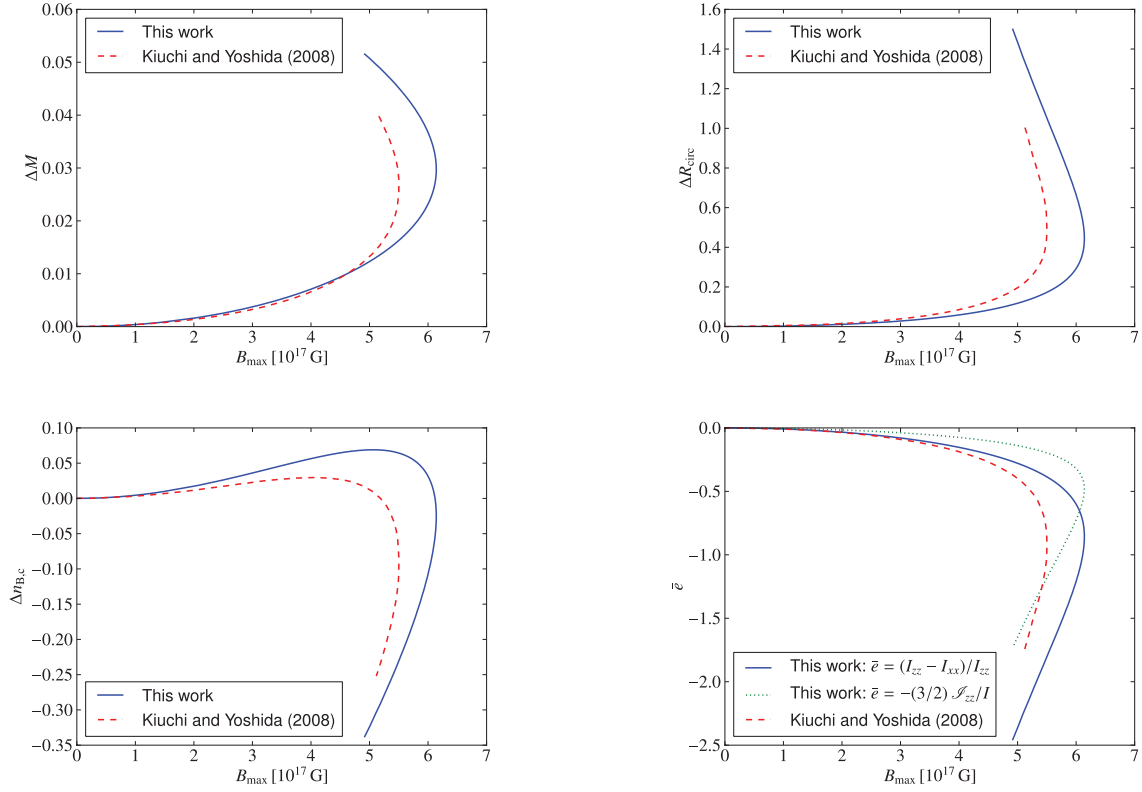
Figure 3. Comparison of the gravitational mass M, circumferential radius R_{circ}, central baryon number density $n_{\text{b,c}}$ and mean deformation $\bar{e}$ along with the maximum magnetic field strength B_{max} attained inside the star as a function of the magnetization parameter λ_0 for a Pol2 EOS model with a baryon mass of $M_{\text{b}} = 1.680 \, M_{\odot}$ and a circumferential radius of $R_{\text{circ}} = 14.30$ km in the unmagnetized case with results of Kiuchi & Yoshida (2008). The relative variation of some quantity χ is defined as $\Delta \chi(B_{\text{max}}, M_{\text{b}}) \equiv (\chi(B_{\text{max}}, M_{\text{b}}) - \chi(0, M_{\text{b}}))/\chi(0, M_{\text{b}})$.

emission of a distorted star because it overestimates corresponding values by about a factor of 2 for this reference model. Similar differences in the values of $\bar{e}$ and ϵ have been found also for the unmagnetized model with a baryon mass of $M_{\text{b}} = 1.780 \, M_{\odot}$ rotating at $\Omega = 3.230 \times 10^3 \, \text{s}^{-1}$ from table IV of Kiuchi & Yoshida (2008); in this case, the respective values of the mean deformation of $\bar{e} = 0.077\,64$ and $0.074\,62$ differ by about 4 per cent, the quadrupole distortion for the same model is $\epsilon = 0.038\,70$ which is again only half of the value of $\bar{e}$.

In addition to the polytropic Pol2 EOS, we have computed non-rotating models for the sample of realistic EOSs discussed in Section 3.6 and for reference models having a gravitational mass of $M = 1.400 \, M_{\odot}$ in the unmagnetized case (basic physical properties of the unmagnetized reference models are collected in Table 5). Because we cannot show equilibrium models for all of these models, we have decided to use as alternative reference EOS the APR one and to complement model `PP-Pol2` at the maximum field strength limit, with the corresponding model `PP-APR`, which nicely illustrates the impact of a prototypical realistic EOS on the resulting equilibrium model.

Fig. 4 shows isocontours of magnetic field strength and baryon number density for model `PP-APR` at the maximum field strength limit, whose physical properties are collected in Table 4 (again, the dimensions of the unmagnetized reference model with a circumferential radius of $R_{\text{circ}} = 11.34$ km are indicated by a grey disc). The maximum magnetic field strength attains a value of $B_{\text{max}} = 8.046 \times 10^{17}$ G in the equatorial plane. Because the APR EOS is stiffer than the Pol2 EOS, the matter distribution appears less condensed and the peaks of the magnetic field have moved slightly

outwards. Moreover, both the surface deformation $\epsilon_s = -0.1176$ and the quadrupole distortion $\epsilon_s = -0.3045$ are larger than the corresponding values of model `PP-Pol2` by ~ 50 per cent. In contrast with model `PP-Pol2`, a substantial fraction of the stellar interior below the surface appears to be field-free. This is easy to understand: according to equation (51), in fact, the amplitude of the toroidal magnetic field is proportional to $(e + p)$, so that the presence of a low-density crust as in the APR EOS suppresses the presence of a toroidal magnetic field in the outer layers of the star.[4] The contour of the unmagnetized reference model not only emphasizes the significant prolate deformation of the maximum field strength model, but also the important increase in the dimensions of the star.

Overall, the non-rotating models built with realistic EOSs show a behaviour which is qualitatively similar to that of the polytropic Pol2 EOS as shown in Table 2 and, for increasing magnetization, all realistic EOS exhibit a maximum value of the magnetic field strength $\langle B^2 \rangle^{1/2}$, beyond which it then decreases. The smallest value is obtained for the GNH3 EOS, with $\langle B \rangle \equiv \langle B^2 \rangle^{1/2} = 2.161 \times 10^{17}$ G; the largest one is instead obtained for the BPAL12 EOS, with $\langle B^2 \rangle^{1/2} = 4.790 \times 10^{17}$ G. Relevant data for all maximum field strength models are collected in Table 2 and reveal that the values of the maximum magnetic field strength decrease with increasing circumferential radii R_{circ}, and which itself is a telltale of the stiffness of the EOS. As a result, the soft BPAL12 EOS with a

---

[4] As customary, we consider the crust not as a solid but as a perfect fluid in analogy with the fluid treatment of the core.
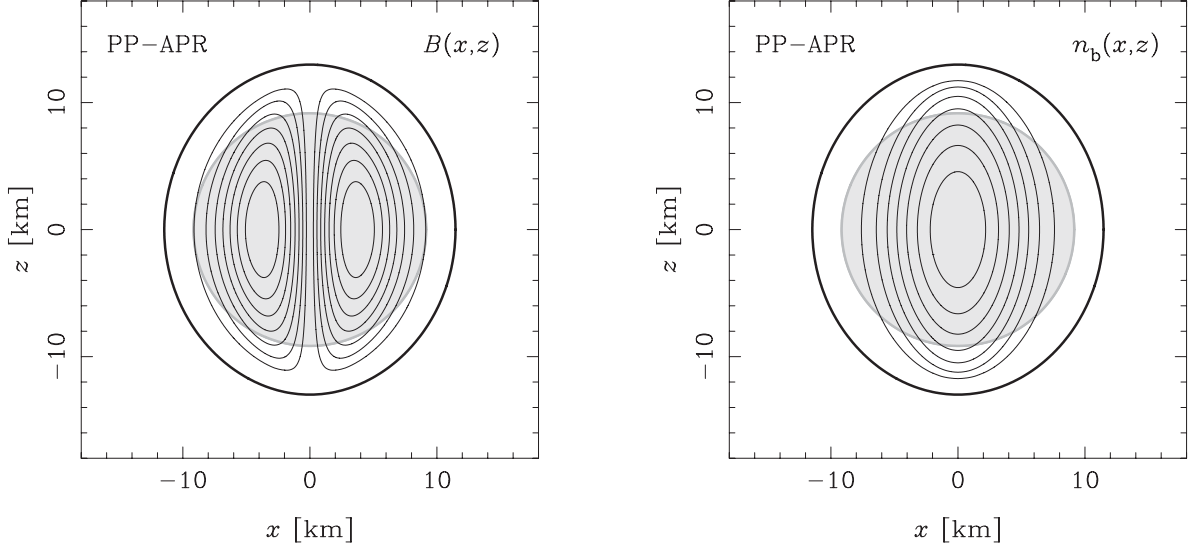
Figure 4. Isocontours of magnetic field strength (left-hand panel) and baryon number density (right-hand panel) in the (x, z) plane of model `PP-APR` of a non-rotating star with a gravitational mass of $M = 1.400\,M_\odot$ and a circumferential radius of $R_{circ} = 11.34$ km in the unmagnetized case built with the APR EOS for a maximum average magnetic field strength of $\langle B^2 \rangle^{1/2} = 3.597 \times 10^{17}$ G. The grey disc indicates the dimensions of the unmagnetized reference model. The physical properties of model `PP-APR` are listed in Table 4.

Table 2. Non-rotating neutron star models computed with different EOSs at the maximum field-strength limit. The gravitational mass is $M = 1.400\,M_\odot$ for each EOS respectively in the unmagnetized and non-rotating case for which properties are listed in Table 5. B_{max} is the maximum value of the magnetic field, $\langle B^2 \rangle^{1/2}$ the root mean square average of the magnetic-field strength determined over the volume of the star, $n_{b,c}$ the central baryon number density ($\times 0.1\,\text{fm}^{-3}$), M the gravitational mass, R_{circ} the circumferential radius, I the moment of inertia, $\mathcal{M}/|W|$ the ratio of the total magnetic energy $\mathcal{M}$ to the potential energy W, ϵ_s the surface deformation, ϵ the quadrupole distortion and GRV2/GRV3 the estimates of the global error of respective models based on the relativistic virial identities introduced in Section 4.3.

EOS	B_{max} $(\times 10^{17}\text{G})$	$\langle B^2 \rangle^{1/2}$ $(\times 10^{17}\text{G})$	$n_{b,c}$ $(\times 0.1\,\text{fm}^{-3})$	M $(M_\odot)$	R_{circ} (km)	I $(\times 10^{38}\,\text{kg m}^2)$	$\mathcal{M}/|W|$	ϵ_s	ϵ	$|\text{GRV2}|$	$|\text{GRV3}|$
Pol2	7.408	2.917	8.409	1.427	14.34	1.278	0.3186	−0.0806	−0.1986	7×10^{-11}	3×10^{-9}
APR	8.046	3.597	6.036	1.438	13.58	1.136	0.2922	−0.1176	−0.3045	5×10^{-7}	4×10^{-7}
BBB2	8.475	3.781	7.132	1.439	13.31	1.093	0.3133	−0.1138	−0.2899	3×10^{-6}	4×10^{-6}
BN1H1	6.414	2.830	7.174	1.432	15.14	1.319	0.2810	−0.1086	−0.3065	2×10^{-5}	2×10^{-5}
BPAL12	12.10	4.790	13.91	1.438	11.83	0.897	0.4589	−0.0782	−0.1729	3×10^{-6}	4×10^{-6}
FPS	9.090	4.019	7.908	1.440	12.99	1.046	0.3308	−0.1122	−0.2809	1×10^{-5}	2×10^{-5}
GNH3	5.090	2.161	4.182	1.427	17.06	1.605	0.1984	−0.1083	−0.3313	5×10^{-6}	1×10^{-5}
SLy4	7.523	3.341	5.972	1.436	14.04	1.191	0.2848	−0.1156	−0.3076	6×10^{-6}	3×10^{-6}

circumferential radius of only $R_{circ} = 11.83$ km yields the model with the highest maximum magnetic field strength, while the stiff GNH3 EOS the model with the lowest one.

We note that in Fig. 3, we have employed the peak magnetic field strength B_{max} and not the average magnetic field strength $\langle B^2 \rangle^{1/2}$, which reaches its turning point already at a lower magnetization level. For this reason, all models based on a realistic EOS are located in a region where $\Delta n_{b,c} > 0$, as can be seen by a comparison with the related values of the unmagnetized models compiled in Table 5. The maximum values of the peak magnetic field strength B_{max} are sensibly larger than those of the average magnetic field strength $\langle B^2 \rangle^{1/2}$, attaining their maximum value for the model built with the FPS EOS with $B_{max} = 1.210 \times 10^{18}$ G.

The slight increase of the gravitational mass is the result of different contributions, which can be illustrated by the example of the `PP-Pol2` model. More specifically, the increase by $0.02682\,M_\odot$ in the gravitational mass of the maximum field strength model with respect to the unmagnetized model. This increase is the sum of a positive contribution of $0.03036\,M_\odot$ due to the total magnetic

energy, of a negative contribution of $-0.02160\,M_\odot$ due to the internal energy lost because of the increased volume, and of a positive contribution of $0.01806\,M_\odot$ by which the magnetized model is less gravitationally bound than its unmagnetized counterpart. Furthermore, all maximum field strength models exhibit smaller moments of inertia than in the unmagnetized case because of the lateral compression of the stellar core. Finally, we note that after reaching a minimum value, the moments of inertia increase continuously with the magnetization, as the growth of the dimensions of the star becomes significant.

The values of the surface deformation ϵ_s and of the quadrupole distortion ϵ obtained for our sample of maximum field strength models also show a noticeable dependence on the stiffness of the EOS. In particular, the value of ϵ decreases (its absolute value increasing) with the increase of the circumferential radius R_{circ}. The Pol2 EOS model appears somehow at variance with this trend, but we believe this is caused by our choice of a comparatively large circumferential radius of $R_{circ} = 12.00$ km in the unmagnetized case, and which does not reflect the rather soft character of this
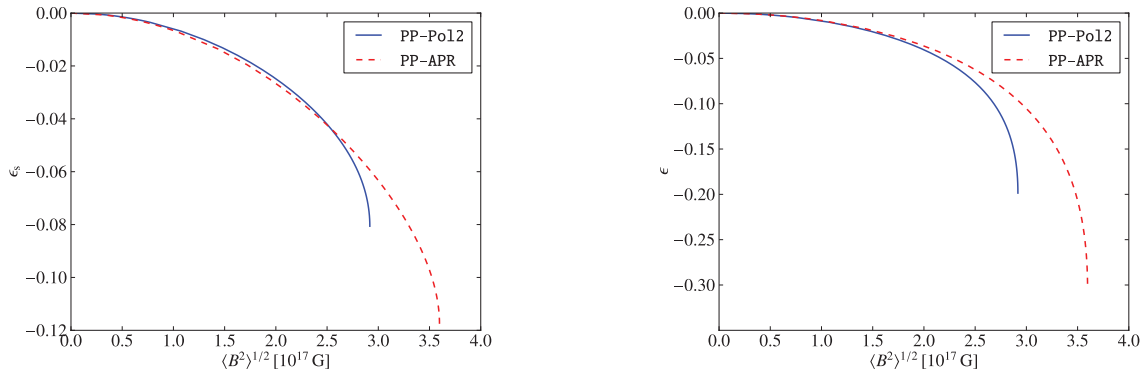
Figure 5. Surface deformation ϵ_s (left-hand panel) and quadrupole distortion ϵ (right-hand panel) for non-rotating models built with the Pol2 EOS and the APR EOS as a function of the root mean square magnetic field strength $\langle B^2 \rangle^{1/2}$ from the unmagnetized limit up to the maximum field strength models `PP-Pol2` and `PP-APR`, respectively. The physical properties of models `PP-Pol2` and `PP-APR` are listed in Table 4.
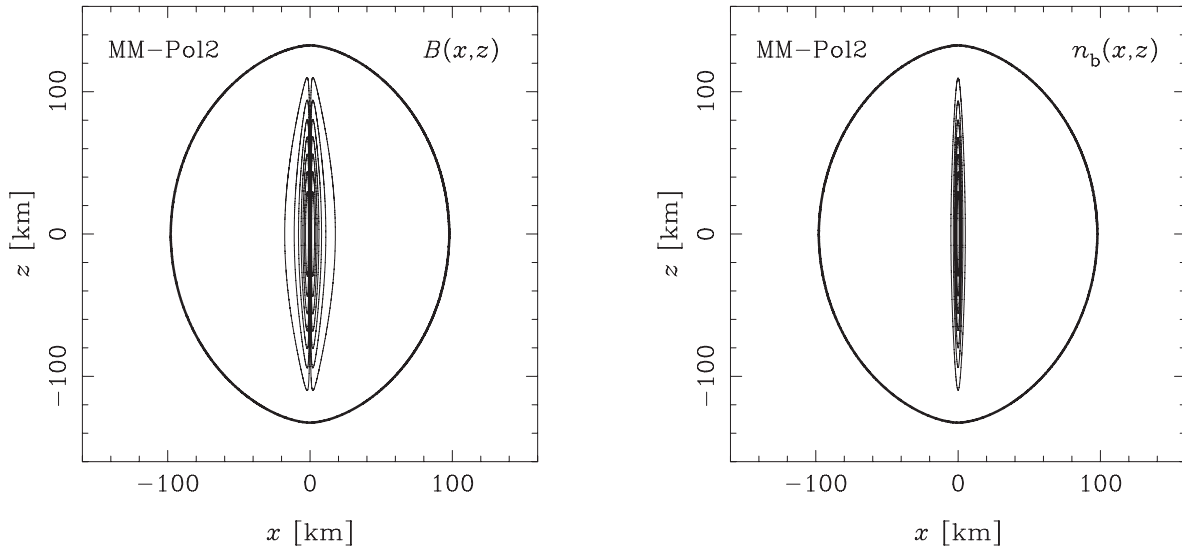
Figure 6. Isocontours of magnetic field strength (left-hand panel) and baryon number density (right-hand panel) in the (x, z) plane of model `MM-Pol2` of a non-rotating star with a gravitational mass of $M = 1.400\,M_\odot$ and a circumferential radius of $R_{\rm circ} = 12.00\,{\rm km}$ in the unmagnetized case built with the Pol2 EOS for an average magnetic field strength of $\langle B^2 \rangle^{1/2} = 0.1400 \times 10^{17}\,{\rm G}$. The physical properties of model `MM-Pol2` are listed in Table 3.

EOS. Lower and upper bounds for the quadrupole distortion are set by the two extremal EOS of our sample: the model built with the soft EOS BPAL12 with a radius of less than 12.00 km exhibits the smallest quadrupole distortion despite of the largest ratio of magnetic energy to binding energy, whereas the large GNH3 model with a radius of 17.06 km shows the largest quadrupole distortion for the lowest ratio of magnetic energy to binding energy of the whole sample.

Much of what discussed so far is summarized in Fig. 5, where we present the dependence of the surface deformation ϵ_s and of the quadrupole distortion ϵ on the average magnetic field strength $\langle B^2 \rangle^{1/2}$, for the representative Pol2 EOS and the APR EOSs. Note that up to $\langle B^2 \rangle^{1/2} \simeq 2.0 \times 10^{17}\,{\rm G}$, the behaviour of both distortions is essentially the same for the two EOSs and an almost perfectly linear function[5] of $\langle B^2 \rangle$. This is not particularly surprising and indeed earlier Newtonian studies (Wentzel 1960; Ostriker & Gunn 1969) have suggested to parametrize the quadrupolar distortion $\epsilon_{\rm Newt}$ induced

in a self-gravitating incompressible fluid by a toroidal magnetic field as a simple function of the ratio of the magnetic energy to binding energy, and hence as a function which is quadratic in the magnetic field strength. Fig. 5 suggests therefore that this behaviour is preserved also in general relativity and up to very large magnetic fields, thus offering the possibility of expressing the magnetically-induced deformation in terms of a simple algebraic expression with coefficients which will correct the previously known Newtonian ones. A more detailed discussion of this point is presented in Section 7 and in Appendix A.

We conclude this section by commenting on a novel and particularly interesting result of our analysis of non-rotating configurations, namely, that no physical or numerical limit was found for the magnetization level. More specifically, after suitably increasing the number of collocation points according to the desired level of accuracy, we were able to find solutions with very large values of the surface and quadrupolar deformations. As an example, we could obtain convergent solutions of the non-rotating reference model of Kiuchi & Yoshida (2008) with a baryon mass of $M_b = 1.680\,M_\odot$ and a circumferential radius of $R_{\rm circ} = 14.30\,{\rm km}$ in the unmagnetized case, now strongly magnetized and attaining a circumferential radius of $R_{\rm circ} = 101.5\,{\rm km}$ and a related value of $\Delta R_{\rm circ} = 6.098$.

---

[5] This is not straightforward to deduce from Fig. 5, which reports ϵ_s and ϵ as a function of $\langle B \rangle$. However, it is very apparent when plotting the distortions as a function $\langle B^2 \rangle$ (not reported here for compactness).
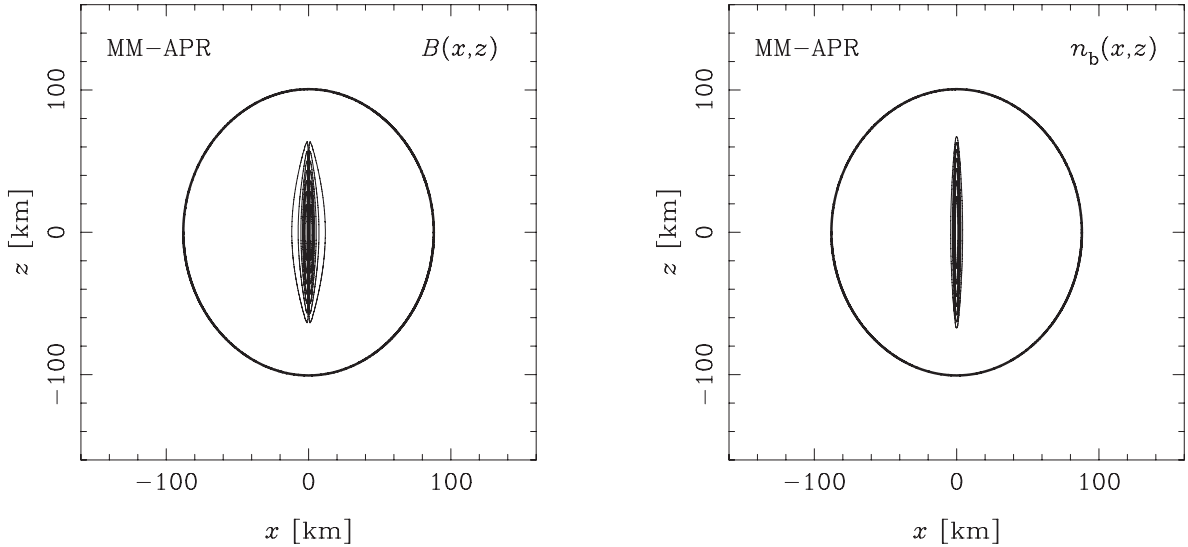
Figure 7. Isocontours of magnetic field strength (left-hand panel) and baryon number density (right-hand panel) in the (x, z) plane of model `MM-APR` of a non-rotating star with a gravitational mass of $M = 1.400\,\mathrm{M}_\odot$ and a circumferential radius of $R_{\mathrm{circ}} = 11.34\,\mathrm{km}$ in the unmagnetized case built with the APR EOS for an average magnetic field strength of $\langle B^2 \rangle^{1/2} = 0.2313 \times 10^{17}\,\mathrm{G}$. The physical properties of model `MM-APR` are listed in Table 3.

While the average magnetic field strength $\langle B^2 \rangle^{1/2} = 0.1461 \times 10^{17}\,\mathrm{G}$ is about an order of magnitude smaller than the maximum value of $\langle B^2 \rangle^{1/2} = 2.241 \times 10^{17}\,\mathrm{G}$ reached at a circumferential radius of $R_{\mathrm{circ}} = 17.09\,\mathrm{km}$, the ratio of magnetic energy to binding energy is much higher with values of $\mathscr{M}/|W| = 0.4868$ and 0.1308, respectively. The surface deformation of this model reaches a value of $\epsilon_s = -0.2403$ and the quadrupole distortion reaches an impressive value of $\epsilon = -6.946$. While clearly unrealistic for ordinary neutron stars, young protoneutron stars may, in principle, attain these magnetizations and possibly these sizes (Villain et al. 2004); clearly, this represents a possibility that deserves a more careful investigation.

In order to illustrate the extreme effects of the toroidal magnetic field at high levels of magnetization, we have computed model `MM-Pol2` of the Pol2 EOS reference model with a gravitational mass of $M = 1.400\,\mathrm{M}_\odot$ and a circumferential radius of $R_{\mathrm{circ}} = 12.00\,\mathrm{km}$ in the non-rotating and unmagnetized case, now inflated to a circumferential radius of $R_{\mathrm{circ}} = 100.0\,\mathrm{km}$. Such an 'extra-large' model is shown in Fig. 6, which, as the previous ones, reports the isocontours of magnetic field strength (left-hand panel) and baryon number density (right-hand panel) for an average magnetic field strength of $\langle B^2 \rangle^{1/2} = 0.1400 \times 10^{17}\,\mathrm{G}$. The physical properties of model `MM-Pol2` are listed in Table 3. In this case, therefore, the surface and quadrupolar deformations reach the extreme values of $\epsilon_s = -0.2609$ and $\epsilon = -7.803$, respectively.

Although new and somewhat surprising, these results are not totally unexpected, and we note that already for a purely poloidal magnetic field, Cardall et al. (2001) doubted the existence of a mass-shedding limit in the non-rotating case. This leads to the conclusion that the non-convergence limit encountered by Kiuchi & Yoshida (2008) at $R_{\mathrm{circ}} = 28.85\,\mathrm{km}$ may be due to their numerical scheme. Furthermore, to confirm that the extreme distortions reported for model `MM-Pol2` are not a peculiarity of the Pol2 EOS, we have found similar equilibria also for model `MM-APR`, built with the APR EOS with a gravitational mass of $M = 1.400\,\mathrm{M}_\odot$ and a circumferential radius of $R_{\mathrm{circ}} = 11.34\,\mathrm{km}$ in the unmagnetized case. This is shown in Fig. 7 and exhibits the same spindle-shaped matter distribution of the stellar core for a circumferential radius of $R_{\mathrm{circ}} = 90.26\,\mathrm{km}$ and

an average magnetic field strength of $\langle B^2 \rangle^{1/2} = 0.2313 \times 10^{17}\,\mathrm{G}$. The physical properties of model `MM-APR` are listed in Table 2, but we note here that the surface and quadrupolar deformations reach the extreme values of $\epsilon_s = -0.1248$ and $\epsilon = -4.810$, respectively. These values are smaller than those of model `MM-Pol2` (despite the ratio of magnetic energy to binding energy is similar and $\mathscr{M}/|W| \approx 0.5$) but shows quite clearly that extremely large deformations are a feature of non-rotating models, independently of the EOS.

6 ROTATING MAGNETIZED MODELS

Having investigated non-rotating models in the previous section, we next turn to models that include rotation, which is well known to induce deformations of the stars that are the opposite of those discussed so far, namely, of introducing an oblateness generically both in the surface deformation and in the quadrupole distortion. In particular, we are concerned with determining the limits of the space of solutions in terms of both the magnetization and the rotation rate. To probe in detail such a space of solutions we consider two rotating models corresponding to maximum field strength configurations of the Pol2 EOS. The first of these reference models, which we refer to as `PO-Pol2`, has a mean magnetic field strength of $\langle B^2 \rangle^{1/2} = 2.324 \times 10^{17}\,\mathrm{G}$ and rotates at an angular velocity of $\Omega = 3.969 \times 10^3\,\mathrm{s}^{-1}$, thus with a moderate ratio of kinetic energy to binding energy of $T/|W| = 0.032\,00$. The second model, which we refer to as `OO-Pol2`, has a mean magnetic field strength of $\langle B^2 \rangle^{1/2} = 1.393 \times 10^{17}\,\mathrm{G}$ and rotates rapidly at an angular velocity of $\Omega = 5.050 \times 10^3\,\mathrm{s}^{-1}$, with a ratio $T/|W| = 0.071\,36$ (see Table 4 for a complete list of the physical properties).

The magnetic field strength and the baryon number density of both models are shown in Fig. 8, with the top row referring to `PO-Pol2` and the bottom one to `OO-Pol2`. The denomination of these two models becomes apparent when considering the corresponding surface and quadrupole deformations. While in fact the qualitative properties of `PO-Pol2` seem to resemble those of the non-rotating model `PP-Pol2`, the surface of this model is markedly flattened and indeed with a positive oblateness of $\epsilon_s = 0.1521$.

Table 3. The same as in Table 2 but for models with large magnetizations of $\mathcal{M}/W \approx 0.5$.

Model	B_{max} ($\times 10^{17}$ G)	$\langle B^2 \rangle^{1/2}$ ($\times 10^{17}$ G)	$n_{\text{b,c}}$ ($\times 0.1$ fm^{-3})	M (M$_\odot$)	R_{circ} (km)	I ($\times 10^{38}$ kg m^2)	$\mathcal{M}/|W|$	ϵ_{s}	ϵ	$|\text{GRV2}|$	$|\text{GRV3}|$
MM-Pol2	2.514	0.1400	1.832	1.508	100.0	9.024	0.5006	−0.2609	−7.803	2×10^{-5}	1×10^{-4}
MM-APR	6.166	0.2313	4.219	1.544	90.26	4.909	0.5095	−0.1248	−4.810	8×10^{-6}	1×10^{-4}

Table 4. Neutron star models at the maximum field strength limit. The gravitational mass is $M = 1.400$ M$_\odot$ for each EOS, respectively, in the unmagnetized and non-rotating case for which properties are listed in Table 5. B_{max} is the maximum value of the magnetic field strength, $\langle B^2 \rangle^{1/2}$ the root mean square value of the magnetic field strength determined over the volume of the star, $n_{\text{b,c}}$ the central baryon number density ($\times 0.1$ fm^{-3}), M the gravitational mass, R_{circ} the circumferential radius, I the moment of inertia, Ω the angular velocity, $T/|W|$ the absolute value of the ratio of total kinetic energy T and potential energy W, $\mathcal{M}/|W|$ the absolute value of the ratio of total magnetic energy $\mathcal{M}$ and potential energy W, ϵ_{s} the surface deformation, ϵ the quadrupole distortion, and GRV2/GRV3 the estimates of the global error of respective models based on the relativistic virial identities introduced in Section 4.3.

Model	B_{max} ($\times 10^{17}$G)	$\langle B^2 \rangle^{1/2}$ ($\times 10^{17}$G)	$n_{\text{b,c}}$ ($\times 0.1$ fm^{-3})	M (M$_\odot$)	R_{circ} (km)	I ($\times 10^{38}$ kg m^2)	Ω ($\times 10^3$ s^{-1})	$T/|W|$	$\mathcal{M}/|W|$	ϵ_{s}	ϵ	$|\text{GRV2}|$	$|\text{GRV3}|$
PP-Pol2	7.408	2.917	8.409	1.427	14.34	1.278	0.000	0.000 00	0.1326	−0.0806	−0.1986	4×10^{-11}	3×10^{-9}
PO-Pol2	5.898	2.324	7.077	1.427	16.35	1.549	3.969	0.032 00	0.1056	0.1521	−0.0684	1×10^{-10}	2×10^{-10}
OO-Pol2	3.264	1.393	5.470	1.424	19.05	1.971	5.050	0.071 36	0.0422	0.5861	0.0856	7×10^{-7}	4×10^{-6}
PP-APR	8.046	3.597	6.036	1.438	13.58	1.136	0.000	0.000 00	0.1754	−0.1176	−0.3045	5×10^{-7}	4×10^{-7}
PO-APR	7.361	3.255	5.861	1.437	14.64	1.247	4.219	0.026 71	0.1494	0.0703	−0.1622	2×10^{-6}	1×10^{-6}
OO-APR	5.548	2.551	5.493	1.432	16.31	1.431	6.004	0.062 76	0.0878	0.4591	0.0072	2×10^{-6}	3×10^{-6}

Table 5. Static reference models without magnetic field and with a gravitational mass of $M = 1.400$ M$_\odot$. $n_{\text{b,c}}$ is the central baryon number density ($\times 0.1$ fm^{-3}), M_{b} the baryon mass, R_{circ} the circumferential radius, I the moment of inertia, b_B the magnetic distortion coefficient defined in equation (73), b_Ω the rotational distortion coefficient defined in equation (73), c_B the magnetic distortion coefficient defined in equation (73), c_Ω the rotational distortion coefficient defined in equation (73), and GRV2/GRV3 the estimates of the global error of respective models based on the relativistic virial identities introduced in Section 4.3.

EOS	$n_{\text{b,c}}$ ($\times 0.1$ fm^{-3})	M_{b} (M$_\odot$)	R_{circ} (km)	I ($\times 10^{38}$ kg m^2)	b_B	b_Ω	c_B	c_Ω	$|\text{GRV2}|$	$|\text{GRV3}|$
Pol2	7.942	1.523	12.00	1.280	5.860×10^{-7}	6.137×10^{-9}	8.338×10^{-7}	2.456×10^{-9}	4×10^{-13}	3×10^{-12}
APR	5.538	1.553	11.34	1.306	6.545×10^{-7}	5.579×10^{-9}	7.922×10^{-7}	2.481×10^{-9}	6×10^{-5}	8×10^{-5}
BBB2	6.368	1.555	11.13	1.256	5.809×10^{-7}	5.229×10^{-9}	6.989×10^{-7}	2.282×10^{-9}	6×10^{-5}	8×10^{-5}
BN1H1	5.018	1.529	12.90	1.590	1.137×10^{-6}	8.215×10^{-9}	1.547×10^{-6}	3.845×10^{-9}	5×10^{-6}	3×10^{-6}
BPAL12	11.88	1.549	10.06	0.971	2.619×10^{-7}	3.528×10^{-9}	3.178×10^{-7}	1.267×10^{-9}	2×10^{-5}	3×10^{-5}
FPS	6.949	1.559	10.85	1.200	4.912×10^{-7}	4.821×10^{-9}	5.798×10^{-7}	2.076×10^{-9}	5×10^{-5}	7×10^{-5}
GNH3	3.654	1.512	14.20	1.814	1.577×10^{-6}	1.078×10^{-8}	2.362×10^{-6}	5.132×10^{-9}	1×10^{-4}	1×10^{-4}
SLy4	5.376	1.546	11.72	1.367	7.422×10^{-7}	6.141×10^{-9}	9.310×10^{-7}	2.756×10^{-9}	9×10^{-5}	1×10^{-4}

The matter distribution inside the star, however, is still prolately deformed, as confirmed by a negative value of the quadrupole distortion, namely $\epsilon = -0.0684$. On the other hand, for model OO-Pol2 both the surface deformation and the quadrupole distortion are positive, i.e. $\epsilon_{\text{s}} = 0.5861$ and $\epsilon = 0.0856$, even though the isocontours of the baryon number density are still prolate towards the centre of the star. Interestingly, for model PO-Pol2, for which the magnetic field is still dominating, the ratio of the magnetic energy to the binding energy $\mathcal{M}/|W|$ exceeds that of the kinetic energy to the binding energy $T/|W|$, whereas for model OO-Pol2, the opposite is true. Hence, while this condition does not hold in all cases, we can take the inequality $\mathcal{M}/T \gtrsim 1$ as a first approximate criterion for the production of a negative quadrupole distortion. A more quantitative discussion on this will be presented in Section 7.

In our sampling of the space of parameters we have computed a total of more than 900 models of rotating and magnetized equilibrium configurations of the Pol2 EOS, which are *uniquely* labelled by the values of the angular velocity Ω and of the magnetization parameter λ_0. The latter extends up to a maximum obtained for a non-rotating model with a radius of $R_{\text{circ}} = 19.45$ km and a ratio of

magnetic energy to binding energy of $\mathcal{M}/|W| = 0.2448$.[6] Overall, the space of physical solutions is delimited by four boundaries: (1) the non-rotating limit with $\Omega = 0$; (2) the unmagnetized limit with $B = 0$; (3) the (self-imposed) 'truncation limit' with respect to the magnetization parameter λ_0; (4) the mass-shedding limit, beyond which no rotating solution does exist.

We have already noted that for non-rotating models the mean magnetic field strength $\langle B^2 \rangle^{1/2}$ is not a monotonic function of the magnetization parameter λ_0 and that after attaining a maximum value of $\langle B^2 \rangle^{1/2} = 2.917 \times 10^{17}$ G, it decreases continuously as the magnetization is increased. This behaviour has been found also for rotating models, thus implying a non-uniqueness for models in the space $(\Omega^2, \langle B^2 \rangle)$. Such a degeneracy could be avoided by replacing the average magnetic field strength with a quantity that grows monotonically with magnetization, e.g. the circumferential radius

---

[6] Note that the 'extra-large' models shown in Figs 6 and 7 are located beyond the truncation limit and thus do not belong to what we consider as the parameter space.
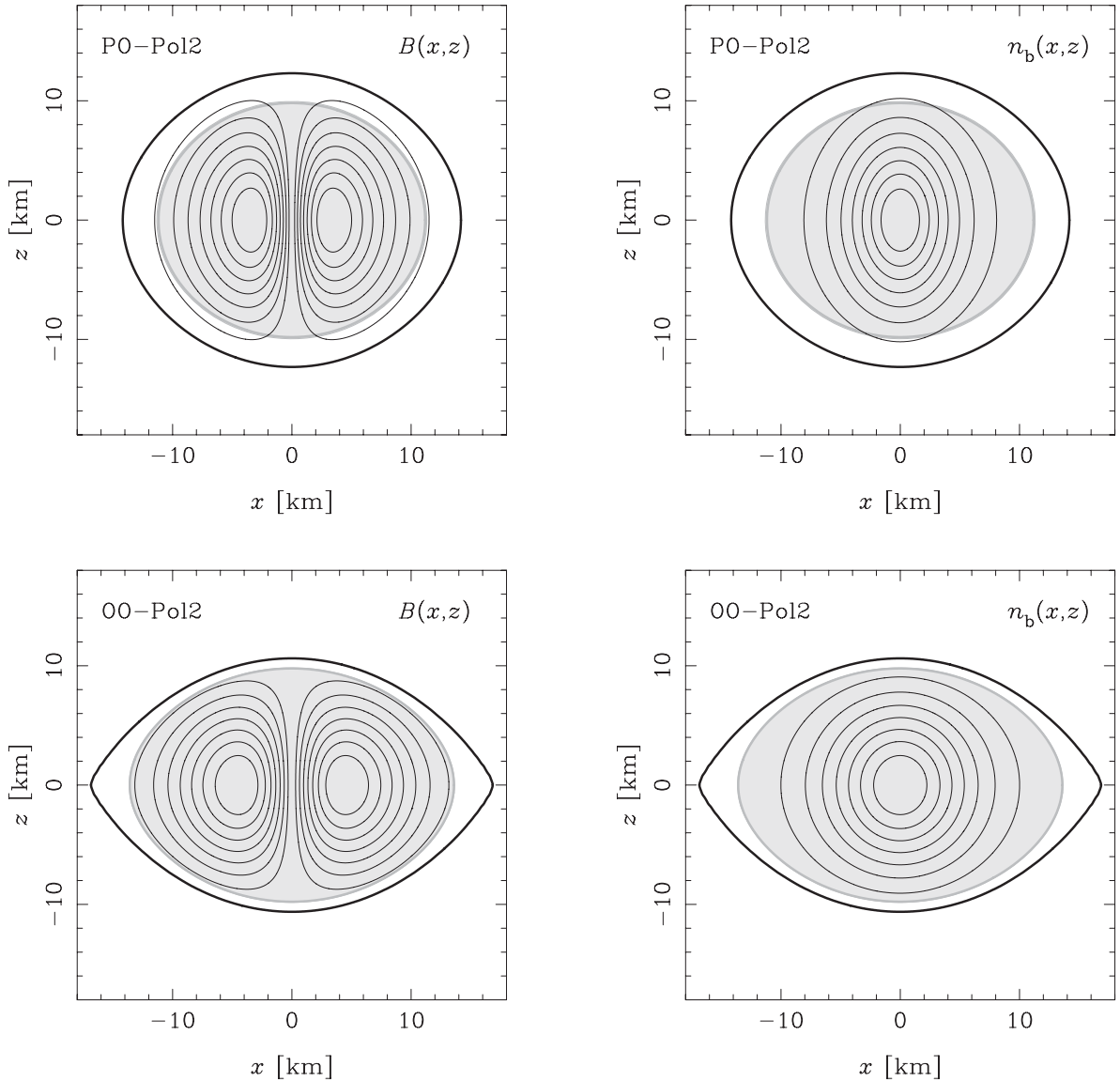
Figure 8. Isocontours of magnetic field strength (left-hand panel) and baryon number density (right-hand panel) in the (x, z) plane of the `P0-Pol2` and `00-Pol2` models of a star, built with a polytropic EOS with $\gamma = 2$ with a gravitational mass of $M = 1.400\,\mathrm{M_\odot}$ and a circumferential radius of $R_{\rm circ} = 12.00$ km in the unmagnetized and non-rotating case, which is now rotating at $\Omega = 3.969 \times 10^3\,\mathrm{s^{-1}}$ (top) and $\Omega = 5.050 \times 10^3\,\mathrm{s^{-1}}$ (bottom), respectively. The grey disc indicates the dimensions of the unmagnetized reference model. The physical properties of models `P0-Pol2` and `00-Pol2` are listed in Table 4.

$R_{\rm circ}$ or the ratio of magnetic energy to binding energy $\mathscr{M}/|W|$. However, because of their fundamental astrophysical importance, we have chosen to report the results for the surface deformation $\epsilon_{\rm s}$ and the quadrupole distortion ϵ in terms of the mean magnetic field strength $\langle B^2 \rangle^{1/2}$ as the ordering quantity and of the angular velocity Ω.

The presence of this degeneracy implies that when evaluated in the space of parameters $(\Omega^2, \langle B^2 \rangle)$, the distortions $\epsilon_{\rm s}$ and ϵ will select a two-dimensional surface which can be split up along the turning points of maximum magnetic field strength into a lower sheet, where $\langle B^2 \rangle^{1/2}$ increases as a function of the magnetization parameter λ_0, and an upper sheet, where the opposite happens. The left-hand panel of Fig. 9, in particular, shows the surface deformation $\epsilon_{\rm s}$ for the lower part of the solution space, while the right-hand panel is its continuation beyond the turning point of $\langle B^2 \rangle^{1/2}$ and thus represents the upper sheet of the surface. Since non-rotating

magnetized models always have a prolate shape, i.e. $\epsilon_{\rm s} < 0$, while rotating unmagnetized models always have an oblate one, i.e. $\epsilon_{\rm s} > 0$, it follows that rotating models between these limiting cases are divided into *prolate* ones and *oblate* ones by a neutral line $\epsilon_{\rm s} = 0$. According to its definition in equation (68), the neutral line $\epsilon_{\rm s} = 0$ does not require the stellar interior to be spherically symmetric and, indeed, when moving towards large values of the circumferential radius $R_{\rm circ}$, models with comparable values of the equatorial and polar coordinate radii $r_{\rm e}$, $r_{\rm p}$ (i.e. with $\epsilon_{\rm s} \to 0$) show a progressively more pronounced 'diamond shape' caused by an increasingly spindle-shaped matter distribution inside the star.

Unlike the magnetic potential, the centrifugal one is not confined to the star, and its influence increases moving away from the axis of rotation, reaching its minimum at the equator of the star. Note that $\tilde{M} = 0$ at the surface of the star, so that the latter is now an isosurface of the function $\nu - \ln \Gamma$ (cf. equation 53). From Fig. 9,

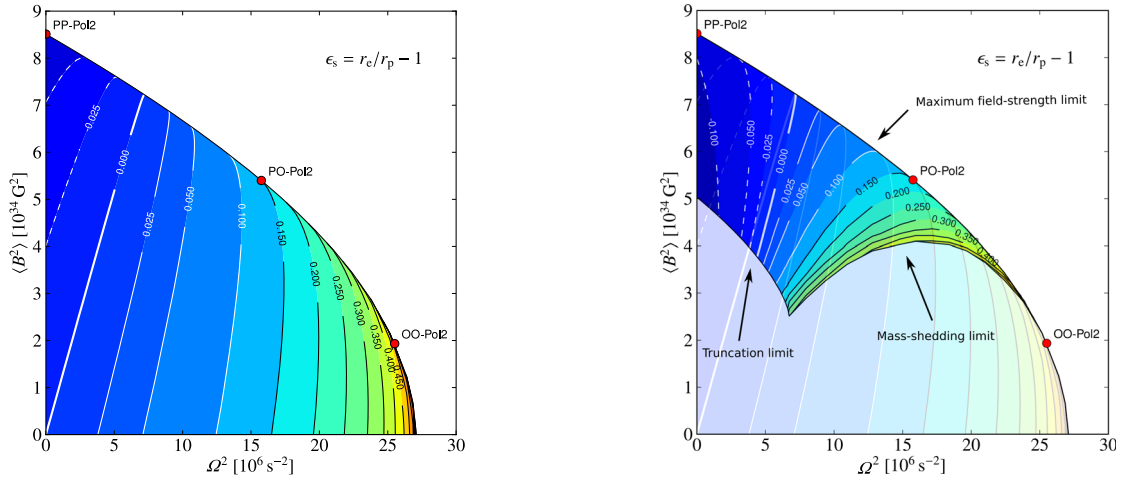**Figure 9.** Isocontours of the surface deformation ϵ_s for the Pol2 EOS reference model with a gravitational mass of $M = 1.400\,M_\odot$ and a circumferential radius of $R_{circ} = 12.00$ km in the unmagnetized and non-rotating case. The curved line which connects the non-rotating model with a maximum average magnetic field strength of $\langle B^2\rangle^{1/2} = 2.917 \times 10^{17}$ G with the unmagnetized model rotating at the mass-shedding limit of $\Omega = 5.205 \times 10^3\,s^{-1}$ separates the lower part of the solution space (left-hand panel) where the mean magnetic field strength increases as a function of the field strength parameter λ_0 from the upper part of the solution space (right-hand panel) where the mean magnetic field strength decreases as a function of the latter. In the right-hand panel, we have also shown the lower sheet lying underneath.

we further infer that for any fixed angular velocity $\Omega \geq \Omega_0$, where $\Omega_0 = 2.594 \times 10^3\,s^{-1}$ is the maximum angular velocity at the magnetization truncation limit, the mass-shedding limit is reached for some oblate shape and $\epsilon_s > 0$. Since the toroidal magnetic field is a source of additional pressure, augmenting the magnetization not only increases the deformation of the surface and of the matter distribution, but it also causes an expansion, particularly of the circumferential radius R_{circ}. At a sufficient level of magnetization, it will therefore be possible to reach the mass-shedding angular velocity, i.e. the rotation frequency such that the condition of geodesic motion at the equator is satisfied, and the star will develop the characteristic cusp at the equator. Because this angular frequency is smaller than the corresponding one for an unmagnetized model having the same rest mass, the toroidal magnetic field indirectly sets a reduced limit of the spin frequency of these objects. In Fig. 9, this mass-shedding limit corresponds to the lower right-hand boundary of the upper part of the solution space (see right-hand panel) and along this limit, the Newtonian condition of geodesic motion, $\Omega^2 R_{circ}^3 = \text{const}$, is fulfilled. Note also that with the exception of the unmagnetized one, all mass-shedding models appear to belong to the upper sheet of the solution space. For models rotating at angular velocities up to that of model OO-Pol2, i.e. $\Omega = 5.050 \times 10^3\,s^{-1}$, we have verified this proposition directly by determining the turning point of $\langle B^2\rangle^{1/2}$; for even more rapidly rotating models for which the numerical determination of the maximum field strength limit has not been conclusive, it is supported by extrapolating the boundary between lower and upper part of the solution space beyond model OO-Pol2 towards the unmagnetized mass-shedding limit.

Using a small set of additional rotating models computed beyond the magnetization truncation limit, we have started exploring the behaviour of the equilibrium models in these rather extreme conditions. Overall, we have found that the angular velocity of mass-shedding models decreases progressively, while the boundary associated with the mass-shedding limit and the neutral line $\epsilon_s = 0$ converge to the point $(\Omega^2, \langle B^2\rangle) = (0, 0)$. These results suggest therefore that the solution at $(\Omega^2, \langle B^2\rangle) = (0, 0)$ in the upper sheet of the space of solutions corresponds to the limit of a non-rotating

model of infinite radius and vanishing mean magnetic field strength. This fascinating suggestion clearly requires a more extensive analysis to be confirmed; we postpone this to a subsequent work.

Fig. 9 also reveals that unlike in the unmagnetized rotating case with the same angular velocity Ω, all magnetized mass-shedding configurations behave qualitatively identically when the magnetization is altered, namely, lowering their magnetization moves them away from the mass-shedding limit. Accordingly, rotation becomes sub-critical, and the characteristic cusp at the equator disappears, which is accompanied by a decrease of the surface deformation. Slowly rotating models pass through different stages as the magnetization is lowered from the mass-shedding limit to the given angular velocity Ω down to the limit of vanishing magnetization. More specifically, we find that (i) below the mass-shedding limit, ϵ_s remains positive, but decreases continuously until the neutral line $\epsilon_s = 0$ is crossed for the first time; (ii) the models then become increasingly prolate because the toroidal magnetic field becomes the principal source of deformation until they reach some negative minimum value of ϵ_s; (iii) as the magnetization is further decreased, ϵ_s increases progressively, and models eventually become oblate again when they cross the neutral line $\epsilon_s = 0$ for a second time, and rotation prevails over a decreasing toroidal magnetic field. For models rotating at moderate angular velocities of $3 \times 10^3 \lesssim \Omega \lesssim 5 \times 10^3\,s^{-1}$, the behaviour is similar to that of slowly rotating ones, except that ϵ_s remains positive, so that the models always exhibit an oblate shape regardless of the level of magnetization. Finally, rapidly rotating models with $\Omega \gtrsim 5 \times 10^3\,s^{-1}$ remain close to the magnetized mass-shedding limit regardless of the magnetization level.

Generally speaking, for any fixed angular velocity Ω, the line $\Omega = \text{const}$ is tangential to exactly one level curve of ϵ_s. The touching point determines the magnetization level for which the surface deformation attains its minimum. For decreasing angular velocity, these minima move to higher magnetizations and smaller values of ϵ_s. The angular velocity Ω' for which the maximum magnetic field strength model exhibits $\epsilon_s = 0.007$ separates rotating models into two groups: (1) models rotating at $\Omega > \Omega'$ are always oblate, and the model of minimum (positive) surface deformation is located in the lower part of the solution space; (2) models rotating at $\Omega <$
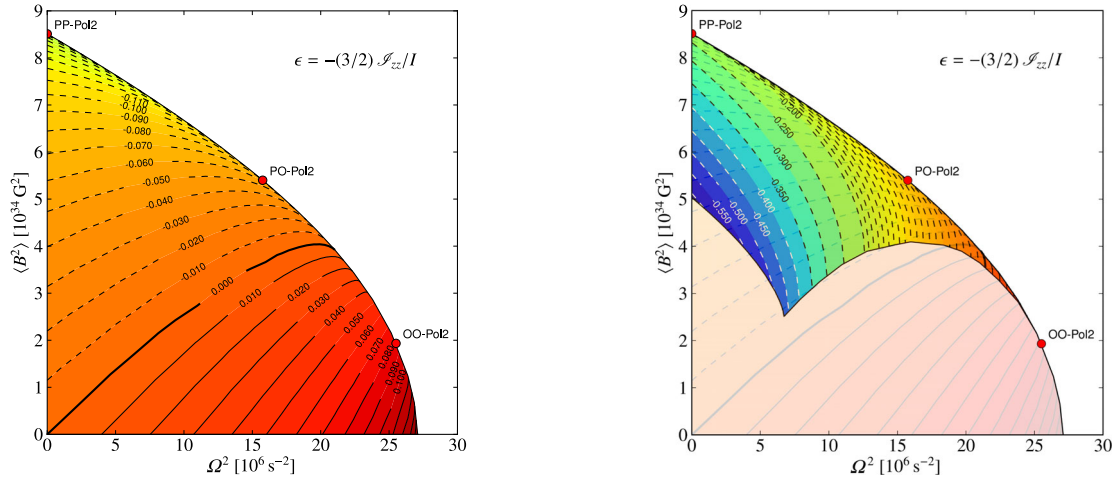
Figure 10. Isocontours of the quadrupole distortion ϵ for the Pol2 EOS reference model with a gravitational mass of $M = 1.400\,\mathrm{M}_\odot$ and a circumferential radius of $R_{circ} = 12.00\,\mathrm{km}$ in the unmagnetized and non-rotating case. The curved line which connects the non-rotating model with a maximum average magnetic field strength of $\langle B^2 \rangle^{1/2} = 2.917 \times 10^{17}\,\mathrm{G}$ with the unmagnetized model rotating at the mass-shedding limit of $\Omega = 5.205 \times 10^3\,\mathrm{s}^{-1}$ separates the lower part of the solution space (left-hand panel) where the mean magnetic field strength increases as a function of the field strength parameter λ_0 from the upper part of the solution space (right-hand panel) where the mean magnetic field strength decreases as a function of latter. In the right-hand panel we have also shown the lower sheet lying underneath.

Ω' include a model of minimum surface deformation $\epsilon_s \leq 0.007$, which is located in the upper part of the solution space.

Fig. 10 provides an equivalent representation of the data shown in Fig. 9 but this time in terms of the quadrupole distortion ϵ. Also in this case, the space of the numerical solutions is split into an upper sheet and a lower one, where the distinction is the same one as made for the surface distortion ϵ_s. For all models, ϵ increases monotonically as a function of the magnetization, and the neutral line $\epsilon = 0$ extends from the non-rotating and unmagnetized reference model, up to a strongly magnetized mass-shedding model with $\langle B^2 \rangle^{1/2} \approx 2 \times 10^{17}\,\mathrm{G}$ rotating at an angular velocity of $\Omega \approx 4.5 \times 10^3\,\mathrm{s}^{-1}$ and with $T/|W| \approx 0.06$. Thus, even rapidly rotating models can exhibit a prolate matter distribution provided the magnetization is sufficiently strong. Although we have truncated the solution space towards high magnetizations, the minimum quadrupole distortion of $\epsilon = -0.6127$, which corresponds to the strongest prolate deformation of our sample and has been obtained for the non-rotating model at the magnetization truncation limit, exceeds considerably the quadrupole distortion $\epsilon = 0.1537$ of the unmagnetized mass-shedding model rotating at $\Omega = 5.205 \times 10^3\,\mathrm{s}^{-1}$ with $T/|W| = 0.09380$. This significant difference can be explained by the large ratio $\mathscr{M}/|W| = 0.2448$ of the magnetized model. Since no mass-shedding limit has been encountered in the non-rotating magnetized case, $\mathscr{M}/|W|$ can possibly attain arbitrarily high values and accordingly, the quadrupole distortion ϵ can, in principle, grow without bounds, too. We leave the assessment of this conjecture to a subsequent work.

We also note that whereas all mass-shedding models exhibit an oblate surface deformation for which $\epsilon_s > 0$, only rapidly rotating mass-shedding models with $\Omega \gtrsim 4.5 \times 10^3\,\mathrm{s}^{-1}$ show a positive quadrupole distortion with $\epsilon > 0$. On the other hand, all mass-shedding models rotating at lower angular velocities actually possess a prolate matter distribution and $\epsilon < 0$ which, moreover, seems to grow without bounds for increasing magnetization like in the non-rotating case. Altogether, Figs 9 and 10 reveal that the neutral lines $\epsilon_s = 0$ and $\epsilon = 0$ differ significantly, suggesting the division of the space of solutions of magnetized and rotating models into

three classes: (1) models for which apparent shape and distortion of the matter distribution are both prolate, thus with $\epsilon_s < 0$ and $\epsilon < 0$, which we label PP for prolate–prolate; (2) models for which the apparent shape is oblate and the distortion of the matter distribution is prolate, thus with $\epsilon_s > 0$ and $\epsilon < 0$, which we label PO for prolate–oblate; (3) models for which apparent shape and distortion of the matter distribution are both oblate, thus with $\epsilon_s > 0$ and $\epsilon > 0$, which we label OO for oblate–oblate. As a result, in contrast with the results of Kiuchi & Yoshida (2008), rotating models with a strong toroidal magnetic field do not necessarily exhibit a negative quadrupole distortion ϵ (cf. discussion in Section 2 and Fig. 1).

Representative models for each of the three classes located at the maximum field strength limit have been presented in Section 5, namely model PP-Pol2, the non-rotating configuration with a prolate apparent shape and a prolate matter distribution, and earlier in this section, namely model PO-Pol2, with a prolate apparent shape and an oblate matter distribution, and model OO-Pol2 with an oblate shape and an oblate matter distribution. Within Figs 9 and 10, their positions in the lower and upper parts of the solution space have been marked by red dots along the line of maximum magnetic field strength related to $\langle B^2 \rangle^{1/2}$. Note that no model exists for which the apparent shape is prolate and the distortion of the matter distribution oblate, i.e. $\epsilon_s < 0$ and $\epsilon > 0$; therefore, because of the different nature of the forces caused by a toroidal magnetic field and rotation, a class OP does not exist. While magnetic and centrifugal forces distort the matter distribution at a comparable level with respect to the involved amounts of magnetic and kinetic energy, the magnetic potential is confined and does not act on the surface of the star directly through equation (53). Therefore, already in the magnetized and non-rotating case, the surface deformation is always smaller than the quadrupole distortion. Moreover, since centrifugal forces act more efficiently at large distances from the rotation axis, their influence on the surface of the star can be significant, and indeed the value of $\epsilon_s = 0.7242$ obtained at the unmagnetized mass-shedding limit is considerably larger (in absolute terms) than the value obtained for the non-rotating model at the upper magnetization limit of $\epsilon_s = -0.1369$; the opposite is true when considering
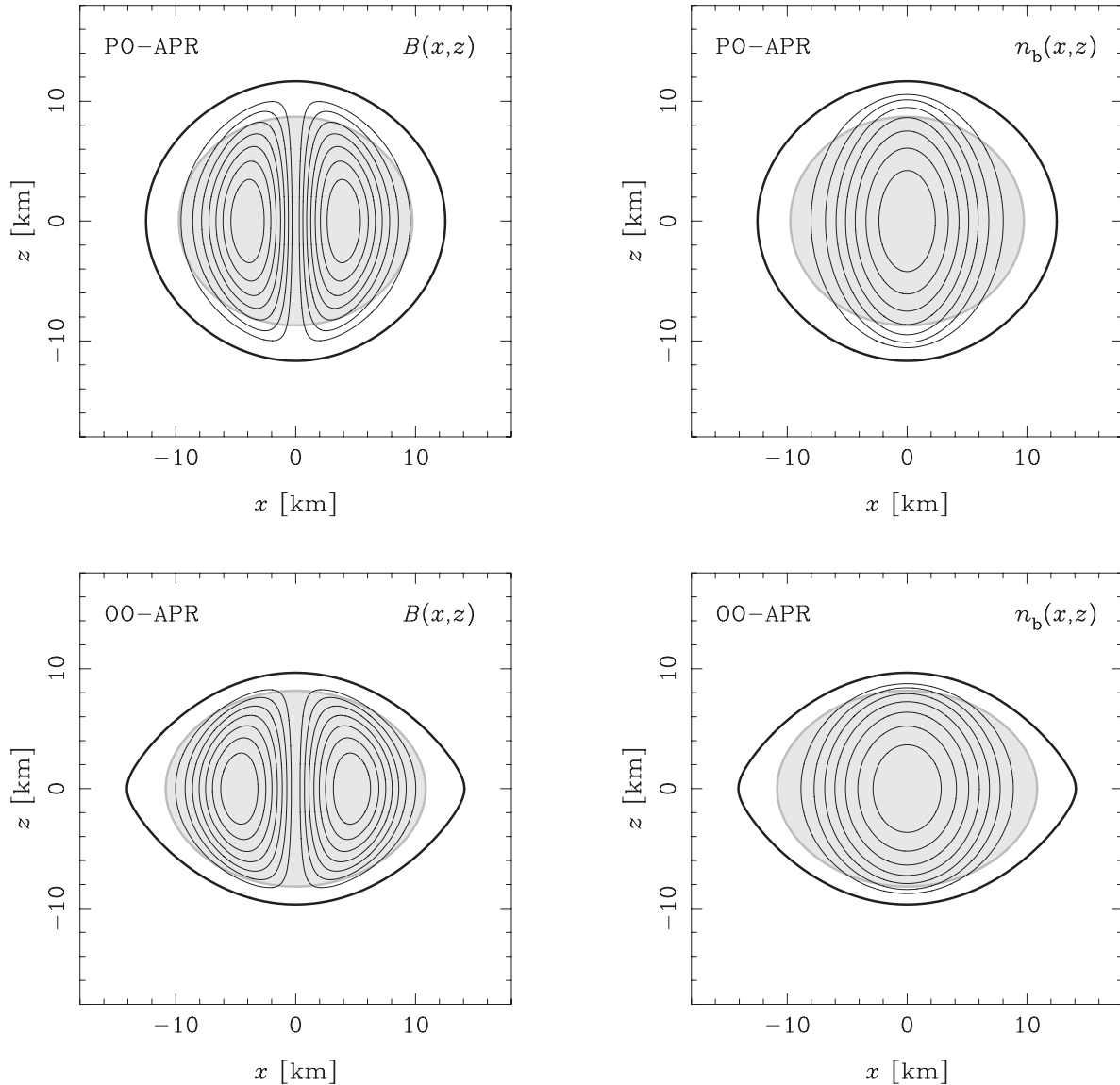
Figure 11. Isocontours of magnetic field strength (left-hand panel) and baryon number density (right-hand panel) in the (x, z) plane of the `PO-APR` and `OO-APR` models of a star, built with the APR EOS with a gravitational mass of $M = 1.400\,M_\odot$ in the unmagnetized and non-rotating case, which is now rotating at $\Omega = 4.219 \times 10^3\,\mathrm{s}^{-1}$ (top) and $\Omega = 6.004 \times 10^3\,\mathrm{s}^{-1}$ (bottom), respectively. The grey disc indicates the dimensions of the unmagnetized reference model. Physical properties of models `PO-APR` and `OO-APR` are listed in Table 4.

the quadrupole distortion with respective values of $\epsilon = -0.6127$ and 0.1537.

In order to assess the general validity of our results obtained in the rotating case for the analytic Pol2 EOS, we have compared the two rotating models `PO-Pol2` and `OO-Pol2` with the corresponding models `PO-APR` and `OO-APR`, built with the APR EOS for identical values of the $T/|W|$ ratio at the unmagnetized limit, i.e. $T/|W| = 0.03$ and 0.07. The physical properties of all models are listed in Table 4, where it is clear that the effects of rotation are less pronounced for the two APR models because of the stiffer nature of the APR EOS. The APR models admit a higher maximum value of $T/|W| = 0.1052$ at the unmagnetized mass-shedding limit, which should be compared with the corresponding $T/|W| = 0.09380$ for the softer Pol2 EOS. Moreover, as discussed in Section 5, the APR EOS reference model supports a higher maximum field strength when compared to the Pol2 EOS one, which causes magnetic effects to be stronger for the two models `PO-APR` and `OO-APR`.

The toroidal magnetic field strength and the baryon number density for the `PO-APR` and `OO-APR` models are reported in Fig. 11, which shows that the matter distributions are less condensed (the EOS is stiffer) and the peaks of the magnetic field strength have moved slightly outward. Their prolate deformation appears more pronounced in agreement with the higher ratio $\mathcal{M}/|W|$, and the outer crust is easily discernible because the magnetic field is essentially absent from this low-density region. The ratio $T/|W|$ for models `PO-APR` and `OO-APR` is smaller than that of their unmagnetized counterparts, in agreement with their smaller moments of inertia. In contrast, models `PO-Pol2` and `OO-Pol2` are already located in the region of increasing moments of inertia and show ratios $T/|W| = 0.03200$ and 0.07119, which are larger than those of the unmagnetized models rotating at the same angular velocities Ω.

Finally, Fig. 12 compares the dependence of ϵ_s and ϵ on the magnetization levels for the four reference rotating models (cf.
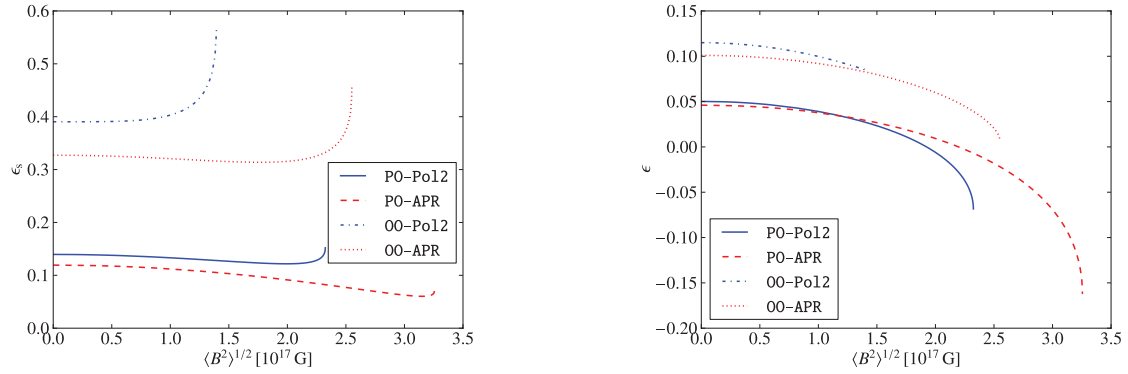
Figure 12. Surface deformation ϵ_s (left-hand panel) and quadrupole distortion ϵ (right-hand panel) for rotating models built with the Pol2 EOS and the APR EOS as a function of the mean square magnetic field strength $\langle B^2 \rangle$ from the unmagnetized limit up to the maximum field strength models `PO-Pol2` and `PO-APR` as well as `OO-Pol2` and `OO-APR`. The angular velocities are chosen such that $T/|W| = 0.03$ and $T/|W| = 0.07$, respectively, in the unmagnetized case.

Fig. 5, where the comparison was made for the non-rotating models `PP-Pol2` and `PP-APR`). Clearly, there is a good qualitative agreement between the two EOSs with differences that are due mostly to the higher maximum magnetic field strength and the higher maximum value of $T/|W|$ supported by models `PO-APR` and `OO-APR`. Note that model `OO-Pol2` is so close to the mass-shedding limit that it is the only one for which models rotating at the same angular velocity Ω show increasing ϵ_s from the unmagnetized limit on. While all sequences in the left-hand panel of Fig. 12 maintain an oblate shape, those associated with models `PO-Pol2` and `PO-APR` show a transition from an oblate matter distribution to a prolate one (right-hand panel of Fig. 12).

7 DISTORTION COEFFICIENTS

Despite the complex behaviour shown by the equilibrium models when both the magnetic field strength and the rotation are varied, it is possible to express such a behaviour through a very simple algebraic expression. This was pointed out already by Wentzel (1960) and Ostriker & Gunn (1969), who have considered this issue in earlier Newtonian studies and have suggested to parametrize the quadrupole distortion $\epsilon_{\rm Newt}$ induced by a toroidal magnetic field and by rotation in a self-gravitating incompressible fluid, respectively, as

$$\epsilon_{\rm Newt} = \epsilon_B + \epsilon_\Omega = -a_B \frac{\mathscr{M}}{|W|} + a_\Omega \frac{T}{|W|}, \qquad (72)$$

where $a_B = a_\Omega = 3.750$. This approximation was adopted also by Cutler (2002) in order to derive an estimate for the quadrupole distortion of neutron stars, within a Newtonian framework. Since neutron stars are highly relativistic objects, we next consider whether an expression similar to equation (72) can be derived in a relativistic regime and the quantitative differences that then emerge with respect to a Newtonian treatment.

We start by recalling that already in Section 6 we have remarked how the surface deformation ϵ_s and the quadrupole distortion ϵ for highly magnetized and rapidly rotating models exhibit an almost linear dependence on Ω^2 and on $\langle B^2 \rangle$. As a result, we can express these quantities in terms of 'deformation coefficients'

$$\epsilon_s = -b_B \langle B_{15}^2 \rangle + b_\Omega \, \Omega^2, \quad \epsilon = -c_B \langle B_{15}^2 \rangle + c_\Omega \, \Omega^2, \qquad (73)$$

where B_{15} expresses the magnetic field strength in units of 10^{15} G and Ω is expressed in s^{-1}. The distortion coefficients b_B, b_Ω for the surface deformation ϵ_s and the coefficients c_B, c_Ω for the quadrupole

distortion ϵ can be easily computed through the directional derivatives along the coordinate axes of Ω^2 and $\langle B^2 \rangle$ and are collected in Table 5 besides the basic properties of the unperturbed models for all of the EOSs considered. The importance of these distortion coefficients is that they provide all the information needed to compute the resulting values of ϵ_s and ϵ by simply inserting appropriate values for the angular velocity Ω and for the mean magnetic field strength $\langle B_{15}^2 \rangle^{1/2}$ in equation (73). In addition, the approximate expressions of equation (73) can cover a very large portion of the physically realistic space of parameters and, for example, in the case of the Pol2 EOS the phenomenological relations yield relative errors $\lesssim 8$ per cent up to values of $\langle B^2 \rangle^{1/2} = 1 \times 10^{17}$ G and angular velocities of $\Omega = 2 \times 10^3$ s^{-1}, which largely cover all known magnetars.

We note that the quadratic dependence expressed by equation (73) applies only to old and cold neutron stars *without* a superconducting proton phase, or to hot protoneutron stars. However, for type II superconducting neutron stars, it has been shown that below the first critical magnetic field strength $H_{c1} \approx 10^{15}$ G, the magnetic field is confined to flux tubes of strength $B_{c1} \approx 10^{15}$ G, which enlarge the anisotropic part of the average electromagnetic stress tensor (Jones 1975; Easson & Pethick 1977) by a factor of H_{c1}/B. As a result, for magnetized models with $\langle B \rangle < 10^{15}$ G, a *linear* dependence of the matter distortion on the average magnetic field strength is expected, and at $\langle B \rangle = 10^{15}$ G, the enhancement factor is $H_{c1}/B = 1$, and this allows us to match the normal-MHD and the superconducting case at this value of $\langle B \rangle$. As a result, equation (73) has to be modified taking the alternate form

$$\epsilon_s = -b_B \langle B_{15} \rangle + b_\Omega \, \Omega^2, \quad \epsilon = -c_B \langle B_{15} \rangle + c_\Omega \, \Omega^2, \qquad (74)$$

In principle, the coefficients appearing in equation (74) should be calculated from the self-consistent equilibrium models of magnetized superconducting relativistic stars, something which is still rather difficult to do. In practice, however, it is possible to take as coefficients the same as those in equation (73), bearing in mind, however, that the corresponding estimates are useful only as a first approximation and as an improvement over the corresponding coefficients by Cutler (2002).

Beyond the second critical magnetic field strength H_{c2}, where $H_{c2} > H_{c1}$, superconductivity is suppressed, and equation (73) applies without restriction yielding the usual quadratic scaling.

Fig. 13 offers a graphical representation of the distortion coefficients for the surface deformation (left-hand panel) and for the quadrupole distortion (right-hand panel). The coefficients b_B and c_B as well as b_Ω and c_Ω are computed for different EOSs and using the reference non-rotating models with a gravitational mass
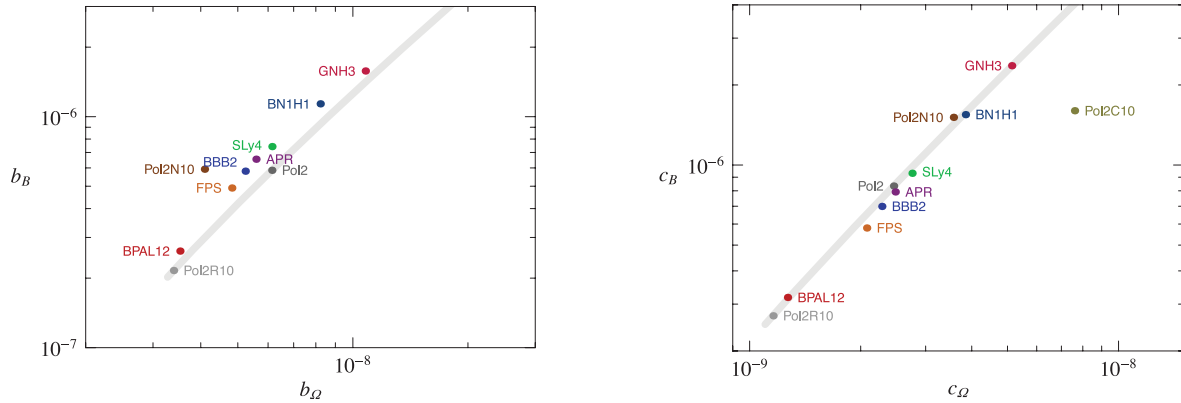
Figure 13. Distortion coefficients b_B and b_Ω for ϵ_s (left-hand panel) as well as c_B and c_Ω for ϵ (right-hand panel) derived in the linear regime by perturbing a non-rotating and unmagnetized star with a gravitational mass of $M = 1.400\,\mathrm{M}_\odot$.

of $M = 1.400\,\mathrm{M}_\odot$. Also shown as a grey-shaded band are the distortion coefficients of non-rotating models with a Pol2 EOS having the same gravitational mass, but where the polytropic constant is varied to obtain different circumferential radii $R_{\rm circ}$ (these have therefore $R_{\rm circ} \geq 9.891\,$km). The influence of the different EOSs is in fact most easily followed through the associated circumferential radius $R_{\rm circ}$, which had already turned out to be a crucial quantity for the maximum field strength models presented in Section 5. As we explain in Appendix A, using basic scaling considerations, the magnetic distortion coefficients exhibit a dependence of the type $b_B, c_B \propto R_{\rm circ}^4$, whereas the rotational distortion coefficients exhibit a dependence of the type $b_\Omega, c_\Omega \propto R_{\rm circ}^3$.

Also shown for comparison in Fig. 13 are the Newtonian reference model from Cutler (2002), labelled `Pol2C10`, and its numerical equivalent as computed with our code in the Newtonian limit, labelled as `Pol2N10`.[7] Note that both Newtonian models have similar values of c_B and that the `Pol2N10` data point is rather close to the reference band of relativistic Pol2 EOS models. However, the rotational distortion coefficient c_Ω reported in Cutler (2002) exceeds the correct Newtonian one of model `Pol2N10` by almost a factor of 2. Furthermore, both data points largely overestimate the correct relativistic result obtained for model `Pol2R10` which is about a factor of 4 smaller and located at the lower end of the relativistic Pol2 EOS. This simple example highlights therefore how a Newtonian treatment is inadequate for the determination of realistic distortion coefficients for real neutron stars.

8 CONCLUSIONS

We have computed models of rotating relativistic stars with a toroidal magnetic field under the assumption that the matter is a single-constituent perfect fluid described by a one-parameter EOS and behaves as a perfect conductor subject to the laws of ideal MHD. We have investigated the combined effects of a toroidal magnetic field and rotation on the apparent shape and on the internal matter distribution, focusing in particular on the quadrupole distortion, as this is the relevant quantity for the gravitational-wave emission. Models of maximum field strength have been computed for a sample of eight different nuclear matter equations of state, together with the surface deformation and the quadrupole distortion.

We have found that non-rotating models appear to admit arbitrary levels of magnetization accompanied by a seemingly unlimited growth of size and quadrupole distortion. In particular, we have been able to compute a highly magnetized model for the Pol2 EOS with a baryon mass of $M_{\rm b} = 1.680\,\mathrm{M}_\odot$, whose circumferential radius of $R_{\rm circ} = 14.30\,$km in the unmagnetized case inflates to $R_{\rm circ} = 101.5\,$km for an average magnetic field of $\langle B \rangle = 0.1461 \times 10^{17}\,$G. These results should be contrasted with those of Kiuchi & Yoshida (2008), who reported a loss of convergence for this model at a moderate level of magnetization and corresponding to a value of merely $R_{\rm circ} = 28.85\,$km.

When considering rotating models we have instead found that the increase in equatorial size introduced by the toroidal magnetic field reduces the frequency at which mass shedding would otherwise appear in unmagnetized models. Overall, the full space of solutions can be split up into three distinct classes for which the surface distortion and the quadrupole distortion are either prolate and prolate, oblate and prolate, or oblate and oblate, respectively.

We have also determined the relativistic distortion coefficients whose absolute value depends mainly on the radius of the star for all the EOSs considered. Using such coefficients it is possible to compute the surface deformation and the quadrupole distortion by means of a simple algebraic expression which is effective for all magnetizations and rotation rates of known magnetars. Finally, a comparison with the corresponding Newtonian distortion coefficients has shown that the latter overestimate the quadrupole distortion induced by the toroidal magnetic field by about a factor of 6 and the one induced by rotation by about a factor of 3. Hence, they are inadequate for strongly relativistic objects like neutron stars.

The results presented here relative to equilibrium configurations provide the first basic steps to explore the stability properties of magnetized stars, whose analysis in full general relativity has recently seen a spur of activity (Ciolfi et al. 2011; Kiuchi, Yoshida & Shibata 2011; Lasky et al. 2011; Ciolfi & Rezzolla 2012; Lasky, Zink & Kokkotas 2012; Zink, Lasky & Kokkotas 2012). We will investigate the stability properties of our models in a forthcoming paper.

---

[7] Only the quadrupole distortion coefficients c_B and c_Ω for model `Pol2C10` were considered by Cutler (2002).

REFERENCES

Akmal A., Pandharipande V. R., Ravenhall D. G., 1998, Phys. Rev. C, 58, 1804

Balberg S., Gal A., 1997, Nucl. Phys. A, 625, 435

Baldo M., Bombaci I., Burgio G. F., 1997, A&A, 328, 274

Bardeen J. M., Piran T., 1983, Phys. Rep., 96, 205

Bocquet M., Gourgoulhon E., Novak J., 1995, A&A, 301, 757

Bombaci I., 1996, in Bombaci I., Bonaccorso A., Fabrocini A., Kievsky A., Rosati S., Viviani M., eds, Perspectives on Theoretical Nuclear Physics. Edizioni ETS, Pisa, p. 223

Bonanno A., Rezzolla L., Urpin V., 2003, A&A, 410, L33

Bonazzola S., 1973, ApJ, 182, 335

Bonazzola S., Gourgoulhon E., 1994, Classical Quantum Gravity, 11, 1775

Bonazzola S., Gourgoulhon E., 1996, A&A, 312, 675

Bonazzola S., Gourgoulhon E., Salgado M., Marck J. A., 1993, A&A, 278, 421

Bonazzola S., Gourgoulhon E., Marck J. A., 1998, Phys. Rev. D, 58, 104020

Cardall C. Y., Prakash M., Lattimer J. M., 2001, ApJ, 554, 322

Carter B., 1970, Commun. Math. Phys., 17, 233

Carter B., 1973, in DeWitt C., DeWitt B. S., eds, Black Holes – Les Houches 1972: Stationary-axisymmetry, Circularity, and the Papapetrou Theorem. Gordon and Breach Science Publishers, New York, p. 159

Ciolfi R., Rezzolla L., 2012, ApJ, 760, 1

Ciolfi R., Ferrari V., Gualtieri L., Pons J. A., 2009, MNRAS, 397, 913

Ciolfi R., Ferrari V., Gualtieri L., 2010, MNRAS, 406, 2540

Ciolfi R., Lander S. K., Manca G. M., Rezzolla L., 2011, ApJ, 736, L6

Colaiuda A., Ferrari V., Gualtieri L., Pons J. A., 2008, MNRAS, 385, 2080

Cutler C., 2002, Phys. Rev. D, 66, 084025

Das M. K., Tandon J. S., 1977, Ap&SS, 49, 277

Douchin F., Haensel P., 2001, A&A, 380, 151

Duncan R. C., Thompson C., 1992, ApJ, 392, L9

Easson I., Pethick C. J., 1977, Phys. Rev. D, 16, 275

Frieben J., Rezzolla L., 2007, Rotating neutron star models with a toroidal magnetic field, Talk at SFB/TR7 Video Seminar, http://wwwsfb.tpi.uni-jena.de/VideoSeminar/Files/20070618-frieben.pdf

Fujisawa K., Yoshida S., Eriguchi Y., 2012, MNRAS, 422, 434

Glendenning N. K., 1985, ApJ, 293, 470

Gourgoulhon E., 2012, Lecture Notes in Physics, Vol. 846, 3 + 1 Formalism in General Relativity. Springer-Verlag, Berlin

Gourgoulhon E., Bonazzola S., 1993, Phys. Rev. D, 48, 2635

Gourgoulhon E., Bonazzola S., 1994, Classical Quantum Gravity, 11, 443

Gourgoulhon E., Haensel P., Livine R., Paluch E., Bonazzola S., Marck J., 1999, A&A, 349, 851

Gourgoulhon E., Markakis C., Uryū K., Eriguchi Y., 2011, Phys. Rev. D, 83, 104007

Gualtieri L., Ciolfi R., Ferrari V., 2011, Classical Quantum Gravity, 28, 114014

Haskell B., Samuelsson L., Glampedakis K., Andersson N., 2008, MNRAS, 385, 531

Haskell B., Samuelsson L., Glampedakis K., Andersson N., 2009, MNRAS, 394, 1711

Ioka K., Sasaki M., 2003, Phys. Rev. D, 67, 124026

Ioka K., Sasaki M., 2004, ApJ, 600, 296

Jones P. B., 1975, Ap&SS, 33, 215

Kiuchi K., Yoshida S., 2008, Phys. Rev. D, 78, 044045

Kiuchi K., Kotake K., Yoshida S., 2009, ApJ, 698, 541

Kiuchi K., Yoshida S., Shibata M., 2011, A&A, 532, A30

Lai D., Rasio F. A., Shapiro S. L., 1993, ApJS, 88, 205

Lander S. K., Jones D. I., 2009, MNRAS, 395, 2162

Lasky P. D., Zink B., Kokkotas K. D., Glampedakis K., 2011, ApJ, 735, L20

Lasky P. D., Zink B., Kokkotas K. D., 2012, preprint (arXiv:1203.3590)

Miketinac M. J., 1973, Ap&SS, 22, 413

Naso L., Rezzolla L., Bonanno A., Paternò L., 2008, A&A, 479, 167

Nozawa T., Stergioulas N., Gourgoulhon E., Eriguchi Y., 1998, A&AS, 132, 431

Oron A., 2002, Phys. Rev. D, 66, 023006

Ostriker J. P., Gunn J. E., 1969, ApJ, 157, 1395

Pandharipande V., Ravenhall D., 1989, in Soyeur M., Flocard H., Tamain B., Porneuf M., eds, NATO ASI Ser. B, Vol. 205, Nuclear Matter and Heavy Ion Collisions. Plenum Press, New York, p. 103

Salgado M., Bonazzola S., Gourgoulhon E., Haensel P., 1994, A&A, 291, 155

Sinha N. K., 1968, Aust. J. Phys., 21, 283

Smarr L., York J. W., Jr, 1978, Phys. Rev. D, 17, 2529

Sood N. K., Trehan S. K., 1972, Ap&SS, 16, 451

Stella L., Dall'Osso S., Israel G. L., Vecchio A., 2005, ApJ, 634, L165

Swesty F., 1996, J. Comput. Phys., 127, 118

Thompson C., Duncan R. C., 1996, ApJ, 473, 322

Thorne K. S., 1980, Rev. Mod. Phys., 52, 299

Tomimura Y., Eriguchi Y., 2005, MNRAS, 359, 1117

Villain L., Pons J. A., Cerdá-Durán P., Gourgoulhon E., 2004, A&A, 418, 283

Wentzel D. G., 1960, ApJS, 5, 187

Yasutake N., Kiuchi K., Kotake K., 2010, MNRAS, 401, 2101

Yasutake N., Maruyama T., Tatsumi T., 2011, J. Phys. Conf. Ser., 312, 042027

Yoshida S., Yoshida S., Eriguchi Y., 2006, ApJ, 651, 462

Yoshida S., Kiuchi K., Shibata M., 2012, Phys. Rev. D, 86, 044012

Zink B., Lasky P. D., Kokkotas K. D., 2012, Phys. Rev. D, 85, 024030

APPENDIX A: ASSESSMENT OF RESULTS BY CUTLER (2002)

As anticipated in Section 7, earlier Newtonian studies have suggested to express the quadrupole distortion ϵ_{Newt} induced in a self-gravitating incompressible fluid by a toroidal magnetic field and by rotation, respectively, as function of the total magnetic energy $\mathscr{M}$, of the kinetic energy T, and of the potential energy W, namely through equation (72) (Wentzel 1960; Ostriker & Gunn 1969). For a spherical star built with a polytropic EOS with $\gamma = 2$ it is easy to estimate that

$$T = \frac{1}{5}\kappa_1 M R^2 \Omega^2 , \ \ W = -\frac{3}{4}\frac{M^2}{R} , \tag{A1}$$

where $\kappa_1 = 0.653\,45$ is a constant derived by Lai, Rasio & Shapiro (1993). As a result, the ratio of the kinetic to binding energy will scale as $T/|W| \propto R^3$. On the other hand, the total magnetic energy $\mathscr{M}$ of the same body reads

$$\mathscr{M} = \frac{1}{8\pi}\int_V B^2 \, \mathrm{d}V \ = \frac{4\pi}{3}R^3\langle B^2 \rangle , \tag{A2}$$

where $\langle B^2 \rangle$ denotes the mean square average of the magnetic field strength B inside the star. It then follows that $\mathscr{M}/|W| \propto R^4$. Eventually, the total distortion ϵ can be expressed in terms of mean magnetic field strength $\langle B^2 \rangle^{1/2}$ and angular velocity Ω, namely (cf. equation 73)

$$\epsilon_{\text{Newt}} = \epsilon_B + \epsilon_\Omega = -c_B \left\langle B_{15}^2 \right\rangle + c_\Omega \, \Omega^2 . \tag{A3}$$

For a Newtonian model with $M = 1.400\,\mathrm{M_\odot}$ and a radius of $R = 10.00$ km, Cutler (2002) has computed c_B according to equations (A1) and (A2) and reported the distortion coefficients as

$$c_B = 1.600 \times 10^{-6} , \quad c_\Omega = 7.600 \times 10^{-9} . \tag{A4}$$

However, if we use equations (A1) and (A2) and adopt an identical model with $M = 1.400\,\mathrm{M_\odot}$ and $R = 10.00$ km, we obtain

$$c_B = 1.610 \times 10^{-6} , \quad c_\Omega = 3.516 \times 10^{-9} , \tag{A5}$$

where $c_\Omega = 6.725 \times 10^{-9}$ for an incompressible fluid. Although the estimates for c_B agree reasonably well, our value for c_Ω is less than half the one quoted in Cutler (2002), which is instead close to

Table A1. Distortion coefficients for a Newtonian star with $M = 1.400\,\mathrm{M_\odot}$ and $R = 10.00\,\mathrm{km}$ for a polytropic EOS with $\gamma = 2$. For comparison, values for an incompressible model with the same properties are included.

γ	a_B	a_Ω	c_B	c_Ω
∞^a	3.750	3.750	2.013×10^{-6}	6.725×10^{-9}
2^b	3.750	3.750	1.610×10^{-6}	3.516×10^{-9}
2^c	3.518	3.804	1.511×10^{-6}	3.569×10^{-9}
2^d	–	–	1.511×10^{-6}	3.567×10^{-9}
2^e	3.750	–	1.600×10^{-6}	7.600×10^{-9}

[a]Distortion coefficients c_B and c_Ω according to equation (72). In the incompressible case, $T = I\Omega^2/2$ with $I = (2/5)MR^2$, and $W = -(3/5)M^2/R$.
[b]As before but using equations (A1) and (A2).
[c]Distortion coefficients derived from the linear perturbation of a numerical Newtonian model.
[d]Distortion coefficients from Haskell et al. (2008) revised by Haskell et al. (2009).
[e]Distortion coefficients from Cutler (2002).

the corresponding value for a homogeneous sphere. To validate our estimates, we have additionally computed the distortion coefficients with our numerical code in the Newtonian limit and obtained

$$c_B = 1.511 \times 10^{-6}, \quad c_\Omega = 3.569 \times 10^{-9}, \tag{A6}$$

which agree well with the estimates from equation (A5). The remaining difference is due to the fact that $a_B = a_\Omega = 3.750$ only in the incompressible case and need to be corrected in the compressible one. After taking into account this EOS dependence, full agreement is achieved, as can be verified in Table A1, which provides a compilation of the different values for the coefficients c_B and c_Ω and where the coefficients a_B and a_Ω have been added when available.

This paper has been typeset from a TEX/LATEX file prepared by the author.